24th EUROPEAN ROTORCRAFT FORUM
Marseilles, France - 15-17 September 1998

REFERENCE: DY10

AEROELASTIC AND DYNAMIC ROTOR RESPONSE WITH ON-BLADE ELEVON CONTROL

Robert A. Ormiston
and
Mark V. Fulton

Army/NASA Rotorcraft Division
Aeroflightdynamics Directorate (AVRDEC)
US Army Aviation and Missile Command
Ames Research Center, Moffett Field, California

A two-blade, 7.5-ft diameter hingeless rotor model with 10% chord on-blade elevons driven by piezoceramic actuators was tested in hover up to 300 ft/sec tip speed and for advance ratios from 0.1 to 0.3 in forward flight at moderate thrust coefficients and successfully demonstrated cancellation and significant reductions of individual 3, 4, and 5/rev blade vibratory flap bending moments. Aeroelastic and structural dynamic response characteristics were evaluated for a wide range of rotor speed and advance ratio using frequency sweep elevon excitation. Simplified and comprehensive analytical models are used to help understand dynamic response including elevon reversal, elevon effectiveness, bending-torsion interaction, and torsion stiffness effects. The comprehensive analysis successfully reproduced the principal characteristics of the experimental results.

1. INTRODUCTION

Significant efforts are now being directed toward on-blade aerodynamic control concepts for reducing helicopter rotor blade and hub vibratory loads, enhancing aerodynamic efficiency, and reducing acoustic signatures, Refs. 1-4. Combined with improving actuation capabilities of smart materials, these approaches hold considerable promise for future advanced rotors. Analytical investigations by Millott and Friedmann, Refs. 5 and 6, and Milgram and Chopra, Refs. 7 and 8, and others, have shown that on-blade aerodynamic control concepts are theoretically practical for reducing rotor vibratory forces and moments transmitted to the fixed system, comparable to higher harmonic control approaches (HHC) that pitch the entire blade from the root. Moreover, the elevon actuator power is significantly less than required for HHC.

Experimental testing of on-blade aerodynamic control concepts has been relatively limited. Consequently, there remains much that is unproved and yet to be understood about these concepts. Early investigations were carried out by Spangler and Hall, Ref. 9, and Chopra et al, Refs. 10 and 11, to demonstrate fundamental concepts including the development of small-scale smart material actuators and to demonstrate operation of on-blade controls in a rotor blade environment.

Recently, the present authors have published experimental results for dynamic response characteristics and vibratory load reductions for a 7.5-ft diameter low-tip-speed rotor with on-blade elevon control surfaces in hover and forward flight, Refs. 12 and 13. These experiments were among the first to demonstrate that smart structure actuation techniques could provide practical levels of elevon deflection at model-scale rotor speed and dynamic pressure conditions and demonstrated, moreover, that such elevon controls could substantially reduce blade vibratory loads in forward flight. The experiments also employed novel testing and data analysis techniques to provide substantial new and unique dynamic response data that illustrate the unusual characteristics of rotors with on-blade elevons (elevon is used herein since terms such as flap, aileron, and servo-flap, are ambiguous or misleading in the present context).

The present paper will address three main objectives. First, the principal results of the hover and forward flight experiments of Refs. 12 and 13

will be presented to demonstrate the rotor response and vibratory load reduction capabilities achieved with on-blade elevon controls and to illustrate the unusual dynamic characteristics of on-blade elevon controls. Second, the reasons for the unique dynamic response characteristics will be investigated with the help of analytical models including parametric studies of the sensitivity of elevon vibratory load effectiveness to blade torsion stiffness. Third, the paper will compare analytical predictions with the experimental data to begin to assess the capability of a current comprehensive analysis to model and predict the aeroelastic and structural dynamics characteristics of rotors with on-blade controls.

Before addressing these objectives, the unique characteristics of on-blade elevon control encountered during the experiments will be briefly introduced and the basic physical phenomena at issue for this paper will be identified.

During the hover experiments of Ref. 12, the quasi-steady blade flap bending moment response to elevon input was observed to first increase and then decrease with rotor speed, approaching a reversal in direction of the response just beyond the nominal operating speed of 760 RPM. Elevon reversal is an aeroelastic phenomenon that occurs when the rotor speed increases to the point where the aerodynamic lift of the elevon is overcome by the opposing lift associated with elastic twist induced by the aerodynamic pitch moment of the elevon. In addition the experimental flap bending moment frequency response showed no evidence of first bending mode resonant response at 760 RPM. A rudimentary static analysis included in Ref. 12 confirmed the observed elevon reversal behavior, but the relationship of elevon reversal to the unusual behavior of the first bending mode frequency response was not explained. Moreover, it was not clear what influence, if any, the elevon reversal phenomena had on the elevon effectiveness for excitation frequencies in the range of interest for control of vibratory loads.

Elevon reversal characteristics are of interest in relation to the servo-flap controlled rotor concept, the on-blade control configuration successfully employed by Kaman helicopters. The servo-flap rotor is based on very low blade torsional flexibility with a correspondingly low servo-flap reversal speed and operates in the 1/rev frequency range to provide vehicle flight control. Conventional wisdom suggests that a low reversal speed might be desirable or even necessary to successfully adapt the on-blade control concept to vibration control in the higher frequency range. If true, this requirement could have significant implications for the design of active on-blade vibration controls.

To help understand the physical mechanisms of elevon reversal and elevon effectiveness, the notions of elevon lift effect and torsion lift effect may be introduced. They refer to the direct lift produced by elevon deflection ($c_{l\delta}\ \delta$) and the indirect and opposing lift produced by blade elastic twist due to the aerodynamic moment of the elevon ($c_{l\alpha}\ \phi$). The elevon lift and torsion lift contributions cancel at elevon reversal; the servo-flap rotor operates beyond the elevon reversal speed via the torsion lift effect, but the relative influence of these two effects at higher frequencies and how they influence the elevon vibratory load effectiveness is more complex and not clear.

Finally, it should be noted that in addition to the phenomena of elevon reversal and the associated mechanisms of elevon lift and torsion lift, the use of on-blade elevons for vibration control must address important traditional rotor structural dynamics considerations - namely, the fundamental interplay of blade bending and torsion mode frequencies with rotor speed, blade stiffness and mass, and the placement of modal frequencies with respect to the N/rev vibratory airload excitation frequencies.

To summarize, the principal dynamics issues to be investigated in this paper are listed as follows. A better understanding of these issues should aid the development of rotor systems using active elevons to control rotor vibratory loads.

1. What is the relationship of elevon reversal to blade flap bending moment response, and how does this influence evolve with excitation frequency?

2. What is the relationship of elevon reversal to elevon effectiveness at frequencies relevant for vibration attenuation?

3. What are the mechanisms by which elevon lift ($c_{l\delta}\ \delta$) and torsion lift ($c_{l\alpha}\ \phi$) determine blade dynamic response and what is the relative importance of elevon lift and torsion lift for elevon vibratory load effectiveness?

4. What bending and torsion frequency placements are favorable? How important is the relationship of the torsion and the second flap bending mode frequencies to elevon effectiveness?

2. MODEL AND TEST DESCRIPTION

2.1 Rotor Blade Construction

The experimental data included in this paper was obtained from hover and wind tunnel tests of a low-tip-speed (300 ft/sec), two-blade, 7.5-ft diameter hingeless rotor with a trailing edge elevon control surface on each blade. The model was tested in the Aeroflightdynamics Directorate Hover Test Chamber as well as the Army/NASA 7- by 10-Foot Wind Tunnel where it is shown installed on the Small-Scale Rotor Test Rig in Fig. 1.

The blades were adapted from available blades to minimize cost and complexity, but the dynamic characteristics were sufficiently realistic to permit exploratory investigation of a number of fundamental aeroelastic, structural dynamic, and vibratory loads characteristics pertinent to active control rotor concepts. The rotor blades are untwisted and uniform in mass and stiffness except at the blade root and the elevon "active section." Chordwise mass and aerodynamic centers are located near the quarter chord of the symmetrical NACA 0012 airfoil section. The blades are constructed of composite materials including a fiberglass spar, foam core, and fiberglass wrapped skin construction. Each blade has two piezoceramic (PZT) bimorph bender beam actuators driving a single, 10% chord, plain elevon with a span of 12% blade radius, centered at the 75% radial location. The actuators are cantilevered to the rear of each blade spar. Fiberglass lever arms project forward from the elevon to engage the tip of the bimorph bender beam to produce elevon rotational motion. A photograph of the actuator and elevon installation is shown in Fig. 2. Flap bending and torsion moment responses were measured with full strain gage bridges located on the blade root flexure at 11.4 % and 12.8% of the blade radius respectively. Additional design and construction details of the blades, actuators, and elevons are available in Ref. 12.

2.2 Rotor Blade Structural Dynamics Characteristics

The fan plot of rotor blade frequencies in the rotating system is shown in Fig. 3 as a function of rotor speed in air at 0 deg collective pitch. The nominal operating speed is 760 RPM (12.67 Hz). These frequencies are analytical predictions of the Second Generation Comprehensive Helicopter Analysis System (2GCHAS), Ref. 14, using blade properties adjusted to match measured frequencies at zero rotor speed. The measured nonrotating blade frequencies were found to be 3.66, 12.0, and 55.6 Hz for flap, chord, and torsion, respectively. Since the blades include the added mass of the elevon actuators but were originally designed for higher tip speed operation, some of the bending frequencies are somewhat different from typical full scale characteristics. At nominal rotor speed the first flap bending frequency is typical for hingeless rotors (1.11/rev). The first lead-lag frequency of 1.08/rev is relatively close to 1/rev. The nominal rotor speed also results in a somewhat unconventional second flap bending mode above 3/rev; this mode is typically below 3/rev. The combination of low torsion stiffness and low nominal rotor speed results in a reasonable first torsion frequency of 4.6/rev. Both the first elevon/actuator and third flap bending frequencies are between 6/rev and 7/rev at nominal rotor speed.

The model was tested over a range of rotor speeds including 200 RPM, 425 RPM, 450 RPM, and 760 RPM (marked on Fig. 3) and thus yielded a variety of dynamic characteristics. At 450 RPM the principal nondimensional frequencies are much increased; the second flap and first torsion frequencies are above 4/rev and 7/rev, respectively. While not representative of typical rotor blades, these alternative natural frequencies afforded a useful opportunity to broaden the fundamental understanding of on-blade elevon control and vibration reduction characteristics.

3. EXPERIMENTAL RESULTS

The purpose of this section is to present the principal experimental results of Refs. 12 and 13 to demonstrate the response characteristics of a rotor with on-blade elevon controls including the unusual characteristics that will be investigated later in the paper and also to demonstrate the vibratory load reduction capabilities achieved with the on-blade elevons.

3.1 Rotor Dynamics in Hover - Frequency Response Functions (FRFs)

As described in Ref. 12, considerable effort was devoted to designing a smart structure actuator and elevon combination that would yield acceptable elevon deflection amplitude under normal operating conditions. The effort was successful and achieved elevon deflections of ± 10 deg for nonrotating conditions and ± 5 deg up to 4/rev at the nominal rotor speed of 760 RPM. This level of elevon performance made it possible to undertake an exploratory investigation of the capability of

an on-blade elevon to generate useful blade flap bending moments and to then study the application of this capability to reduce blade vibratory loads

The presence of an aerodynamic control surface mounted on the blade *in the rotating system* provided a unique opportunity to study the aeroelastic and structural dynamic characteristics of the elevon/rotor blade system. Dynamic response characteristics were primarily determined using frequency sweep excitation of the elevon actuator. The measured elevon deflection and blade response output were analyzed with the CIFER® (Comprehensive Identification from FrEquency Responses) software, Refs. 15 and 16. This post-processing generated frequency response functions (FRFs) of the blade root flap bending and torsion moments to elevon deflection. Time histories from the two blades were averaged to obtain the response of an "average" blade.

The flap bending moment FRF defines the effectiveness of the on-blade control surface for generating blade flap bending moments. These are the *induced* vibratory blade loads required to cancel the uncontrolled steady-state vibratory blade loads of a rotor producing lift and propulsive force in forward flight. While the uncontrolled vibratory blade loads occur only at harmonic frequencies, and elevon effectiveness is mainly important for only those frequencies, the full FRF provides a broader understanding of rotor blade dynamics and how elevon effectiveness is related to important blade dynamic characteristics, e.g. blade natural frequencies, possible antiresonances, etc.

The experimental frequency response functions (FRFs) of torsion and flap bending moment to elevon input are shown in Figs. 4 and 5 for several rotor speeds in the hover operating condition. The magnitude of the torsion moment response exhibits behavior similar to a simple single-degree-of-freedom system and the response peaks at the torsion mode natural frequency; for 760 RPM, the peak response is approximately five times the steady-state response; at lower rotor speeds, the ratio is even higher. The torsion response away from resonance increases substantially with rotor speed. Small interactions between torsion and flap bending are observed at the second and third flap mode frequencies.

The flap bending moment FRFs in Fig. 5 show the resonant peaks at the first three flap bending mode natural frequencies. The effects of rotor speed and aerodynamics are very significant; for example, from zero to 760 RPM, the resonant peak of the second flap bending mode increases by a factor of roughly 20. The third flap bending mode is much less sensitive to rotor speed and, at 760 RPM, the response is smaller than for the second flap mode. Apart from the increase in dynamic pressure with rotor speed, this behavior reflects the effect of the second flap bending mode frequency moving closer to the torsion mode as rotor speed increases while the third flap bending mode moves away.

The behavior of the first flap bending mode in Fig. 5 is a little more unusual than the higher bending modes. At 760 RPM, the response of flap bending moment nearly vanishes at low frequencies, with no evidence of the first flap mode resonance. The behavior at zero frequency was attributed in Ref. 12 to the onset of elevon reversal, but the influence of elevon reversal on dynamic response at higher frequencies such as the first flap bending mode was not clear. The behavior of the flap bending moment response at low frequencies for 200 and 425 RPM is also unusual as it appears roughly proportional to excitation frequency up to about the first flap mode frequency.

Although the torsion mode resonant response is prominent in the torsion moment FRF, and torsion is a significant excitation (torsion lift effect) for flap bending, it is interesting that the torsion mode resonant response is hardly discernible in the flap bending moment FRFs; only a small peak can be seen at 55 Hz for the 425 RPM rotor speed data in Fig. 5. More evidence of this response will be visible in the analytical results.

The flap bending and torsion moment FRF phase angle measurements corresponding to the FRF magnitudes in Figs. 4 and 5 will be introduced later in the paper for comparison with the analytical results.

3.2 Forward Flight Vibratory Loads Reduction

The significant levels of elevon-generated flap bending moment measured in the hover experiments suggested that on-blade elevon control could be effective for reducing vibratory blade loads in forward flight. This led directly to the wind tunnel experiments (Ref. 13) to investigate dynamic response characteristics in forward flight and to determine the capability for vibratory blade loads reduction.

The basic concept of on-blade controls is that blade loads generated by elevon excitation at an integer harmonic of rotor speed will cancel the uncontrolled steady-state periodic vibratory load

at the same frequency if the amplitude and phase of the elevon excitation are properly selected. To investigate how well this would work with the present rotor model, phase sweeps of elevon motion excitation were performed at discrete harmonic frequencies according to the following procedure.

First, a trimmed flight condition was established for a particular collective pitch, with cyclic pitch adjusted to minimize the 1/rev flap bending moment, and with steady-state vibratory loads measured to establish a baseline to evaluate the effectiveness of elevon excitation. Next, voltage excitation was applied to the PZT bimorph actuator to drive the elevon motion at a frequency equal to a discrete integer harmonic of the rotor speed (from 1/rev to 5/rev). These discrete frequency excitations were applied at specific phase angles with respect to the blade azimuth position. A phase sweep of excitations was then performed for each integer harmonic frequency, acquiring a data point for each of a series of elevon excitation phase angles. For each test point, the amplitude of the response was obtained using an FFT of the response at the frequency of the applied voltage. This phase sweep data provided a measurement of elevon effectiveness and enabled identification of the elevon phase required to minimize a flap bending moment harmonic.

Results of the phase sweeps are shown in Figs. 6 and 7 for 760 RPM (collective pitch θ_o = 4 deg and advance ratio μ = 0.2) and show how the flap bending moment amplitudes vary with elevon phase for 2/rev and 3/rev voltage excitation, respectively. The straight lines indicate the baseline steady-state amplitudes for zero excitation voltage (uncontrolled). The data points represent the total combined bending moment (steady-state plus induced) at different elevon phase angles for a sinusoidal PZT actuator excitation voltage and show large changes in the total flap bending moment amplitude caused by the elevon-induced moment. Note that although the two blades show significantly different baseline uncontrolled responses (caused by structural and aerodynamic differences between blades, see Ref. 12), both blades show significant sensitivity to the elevon motion. Note that the 3/rev elevon motion provides a nearly complete cancellation of the 3/rev flap bending moment for a phase of about 90 deg. Note that during the phase sweep excitations, the amplitude of excitation was not specifically chosen at the particular level required for cancellation of the vibratory loads. Additional results were included in Ref. 13 for additional harmonics and excitation amplitudes. Blade root torsion results for the phase sweeps were included as well.

Beyond direct observation of the impact on vibratory loads, the data obtained from the elevon excitation phase sweeps can be used to determine the elevon effectiveness or response derivatives (magnitude of bending moment per degree elevon deflection) as was done in Ref. 13 by using a simple superposition model. This model assumes that the amplitude of the total blade root flap bending moment at each integer multiple harmonic of the rotor speed is the result of a superposition of two components: the steady-state vibratory flap bending moment component and the elevon-induced flap bending moment component with amplitude independent of azimuth (a reasonable assumption for low to moderate advance ratios and for harmonic components above 1/rev). By using the known baseline amplitude and phase, the amplitude and phase of the elevon-induced moment can be identified from the measured data. The success of this approach can be judged by the excellent agreement in Figs. 6 and 7 between the original measured data (denoted in figures by discrete symbols) and the flap bending moment reconstructed using the identified elevon-induced moment (continuous lines).

The phase sweep data for an advance ratio of 0.2 was processed as described above for both 450 RPM and 760 RPM (θ_o = 6.25 and 4 deg, respectively) to yield the direct, elevon-induced flap bending moments for 1/rev - 5/rev applied voltages. These results are summarized for blade 1 and presented in the form of bar charts in Figs. 8 and 9. Both the uncontrolled baseline harmonics and the elevon-induced harmonics of flap bending moment are included. For ease of comparison, each harmonic of the elevon-induced moments has been scaled for ± 5 deg elevon motion.

Consider first the flap bending moments at 760 RPM, Fig. 8. Comparing the amplitudes of each elevon-induced harmonic to its corresponding uncontrolled (baseline) harmonic provides an indication of elevon effectiveness with respect to its capability for canceling that component of the baseline vibratory load. At this flight condition (μ = 0.2 and θ_o = 4 deg), elevon effectiveness is sufficient to cancel the flap bending moment at all harmonics except 2/rev.

The flap bending moment results for 450 RPM (μ = 0.2 and θ_o = 6.25 deg) in Fig. 9 show reduced elevon effectiveness compared with the 760 RPM. In this case the elevon capability is only sufficient to cancel the 5/rev steady-state vibratory load

harmonic and the effectiveness for 3/rev is nearly zero. This difference can be attributed mainly to reductions in elevon effectiveness, rather than increases in the baseline vibratory loads due to increased collective pitch, or changes in dynamic response to airloads (the second flap bending mode is above 4/rev at 450 RPM). The flap bending FRFs are helpful in understanding this influence. As seen in Fig. 5, changes in the structural dynamic response with reduced rotor speed significantly reduce elevon effectiveness, both due to the lower dynamic pressure and due to shifting of the modal frequency resonances. Note, for example, the significant loss of effectiveness for the 3/rev harmonic at 450 RPM due to an apparent antiresonance at 22.5 Hz in Fig. 5.

4. ANALYTICAL MODELS

The objectives of this paper include using analytical models to help interpret the unique phenomena observed in the experimental results and using comparisons with the experimental data to evaluate basic capabilities of the analytical models. Two different analytical models used for these purposes will be described in the next sections.

4.1 Rigid Blade 2-DOF Model

A simplified rigid blade model is useful for investigating basic characteristics of static and dynamic response in hover, including elevon reversal and dynamic coupling of the torsion and first flap bending modes; the development of the equations is briefly outlined here. For simplicity the model uses quasi-steady 2-D strip theory aerodynamics without any unsteady wake effects. A single blade is modeled as a rigid body with flap (β) and torsion (ϕ) rotation degrees of freedom having hinges and restraint springs (K_β and K_ϕ) located at the center of rotation. The blade aerodynamic flap and torsion hinge moments are obtained by integrating the blade lift and moment per unit length (given in terms of blade chord c, dynamic pressure q, and the airfoil lift and moment coefficients c_l and c_m) along the blade length as given by:

$$M_{\beta_a} = \int_0^R (q\, c_l\, c)\, r\, dr$$
$$M_{\phi_a} = \int_0^R (q\, c_m\, c^2)\, dr \qquad (1)$$

where

$$c_l = c_{l\alpha}\left(\phi - \frac{\dot\beta}{\Omega}\right) + c_{l\delta}\,\delta \qquad (2)$$

$$c_m = c_{m\delta}\,\delta + c_{mq}\,\bar c\,\frac{\dot\phi}{\Omega} \qquad (3)$$

where $c_{l\alpha}$ (also written as a) and c_{mq} are the airfoil lift and moment coefficient derivatives for angle of attack and pitch rate respectively and $c_{l\delta}$ and $c_{m\delta}$ are the lift and moment coefficient derivatives for elevon deflection. The dimensionless chord is defined as $\bar c = c/R$. After integration and taking into account the inboard and outboard radial locations of the elevon, r_i and r_o, the aerodynamic moments become:

$$M_{\beta_a} = \frac{\gamma\, I\, \Omega^2}{8}\left[\phi - \frac{\dot\beta}{\Omega} + A_4\,\frac{c_{l\delta}}{a}\,\delta\right] \qquad (4)$$

$$M_{\phi_a} = -\frac{\gamma\, I\, \bar c\, \Omega^2}{6}\left[A_3\,\frac{c_{m\delta}}{a}\,\delta + \frac{3}{2}\,\frac{c_{mq}}{a}\,\bar c\,\frac{\dot\phi}{\Omega}\right] \qquad (5)$$

where γ is the blade Lock number, I is the flapping inertia, and A_3 and A_4 are elevon geometry constants that reflect the aerodynamic contribution of the elevon to the torsion and blade flap bending moments and depend upon the spanwise length and radial location of the elevon. They are defined as follows

$$A_3 \equiv \left(\bar r_o^3 - \bar r_i^3\right) \text{ and } A_4 \equiv \left(\bar r_o^4 - \bar r_i^4\right) \qquad (6)$$

After including the customary inertial, centrifugal, hinge spring stiffness and damping terms, the final 2-DOF equations, following Laplace transformation to the variable s, become:

$$\begin{bmatrix} \left(s^2 + \frac{\gamma}{8}\Omega\, s + p^2\,\Omega^2\right) & -\frac{\gamma}{8}\Omega^2 \\ 0 & \left(s^2 + C\, s + q^2\,\Omega^2\right) \end{bmatrix} \begin{Bmatrix} \beta \\ \phi \end{Bmatrix} = \frac{\gamma\,\Omega^2}{6\,a} \begin{Bmatrix} \frac{3}{4}\,A_4\, c_{l\delta} \\ \frac{\bar c}{\bar I_\phi}\,A_3\, c_{m\delta} \end{Bmatrix} \delta \qquad (7)$$

where

$$C = 2\,\eta_\phi\,\omega_\phi + \frac{\gamma}{4}\,\frac{\bar{c}^2}{\bar{I}_\phi}\,\frac{c_{mq}}{a}\,\Omega\,, \quad \bar{I}_\phi = \frac{I_\phi}{I}$$

$$p^2\,\Omega^2 = \Omega^2 + \omega_\beta^2\,, \quad q^2\,\Omega^2 = \Omega^2 + \omega_\phi^2$$

$$\omega_\beta^2 = \frac{K_\beta}{I}\,, \quad \omega_\phi^2 = \frac{K_\phi}{I_\phi}$$

Additional parameters introduced here are the nonrotating flap bending and torsion frequencies, ω_β and ω_ϕ, the torsion inertia, I_ϕ, and torsion structural damping, η_ϕ. As may be seen, the torsion equation is uncoupled from the flap bending equation and acts as a forcing function for flap bending response. These equations will be used to generate numerical results for exploring dynamic response characteristics in later sections.

The rigid blade equations may be used to obtain closed form solutions for the steady-state torsion and flap bending response. These results may then be used to derive the expressions that describe elevon reversal characteristics. Without the time dependent terms, Eq. (7) may be solved to yield:

$$\left.\frac{\phi}{\delta}\right|_{SS} = -\frac{\gamma}{6}\,\frac{\bar{c}}{\bar{I}_\phi}\,A_3\,\frac{c_{m\delta}}{c_{l\alpha}}\,\frac{\Omega^2}{\Omega^2 + \omega_\phi^2} \tag{8}$$

$$\left.\frac{\beta}{\delta}\right|_{SS} = \frac{\gamma}{8\,p^2}\left[A_4\,\frac{c_{l\delta}}{c_{l\alpha}} + \left.\frac{\phi}{\delta}\right|_{SS}\right] \tag{9}$$

Substituting Eq. (8) into Eq. (9) yields:

$$\left.\frac{\beta}{\delta}\right|_{SS} = \frac{\gamma}{8\,p^2}\,A_4\,\frac{c_{l\delta}}{c_{l\alpha}}\left[1 - \frac{\Omega^2}{B\left(\Omega^2 + \omega_\phi^2\right)}\right] \tag{10}$$

where

$$B = \frac{6\,\bar{I}_\phi}{\gamma\,\bar{c}}\left(\frac{A_4}{A_3}\right)\frac{c_{l\delta}}{c_{m\delta}}$$

The elevon reversal rotor speed is defined by the condition when the flap bending response vanishes (reverses sign). Equation (10) may be solved to yield

$$\Omega_R = \sqrt{\frac{B}{1-B}}\;\omega_\phi \tag{11}$$

The elevon reversal rotor speed is shown to be simply related to the nonrotating torsion frequency. The parameter B primarily depends on the ratio of the elevon lift and moment coefficient derivatives, $c_{l\delta}$ and $c_{m\delta}$, and the elevon constants A_3 and A_4. For typical elevon geometry, the ratio of these constants is on the order of 1.0. For blades with typical inertia properties, B is generally much less than unity and the elevon reversal speed varies with the square root of B. For typical full scale rotor blades, the elevon reversal speed is on the order of the nominal rotor speed.

The static torsion and flap bending response equations may be written in compact form by incorporating the elevon reversal speed from Eq. (11) and normalizing rotor speeds and frequencies by the nominal rotor speed as follows:

$$\left.\frac{\phi}{\delta}\right|_{SS} = -A_4\,\frac{c_{l\delta}}{c_{l\alpha}}\left[\frac{\left(\bar{\Omega}^2/\bar{\Omega}_R^2\right)}{1 + B\left(\bar{\Omega}^2/\bar{\Omega}_R^2 - 1\right)}\right] \tag{12}$$

$$\left.\frac{\beta}{\delta}\right|_{SS} = \frac{\gamma}{8}\,A_4\,\frac{c_{l\delta}}{c_{l\alpha}}\,\frac{\bar{\Omega}^2}{\left(\bar{\omega}_\beta^2 + \bar{\Omega}^2\right)}\left[1 - \frac{\left(\bar{\Omega}^2/\bar{\Omega}_R^2\right)}{1 - B\left(1 - \bar{\Omega}^2/\bar{\Omega}_R^2\right)}\right] \tag{13}$$

where $\bar{\Omega} = \Omega/\Omega_o$, $\bar{\Omega}_R = \Omega_R/\Omega_o$, and $\bar{\omega}_\beta = \omega_\beta/\Omega_o$. Equations (12) and (13) succinctly express the static blade response in terms of the normalized rotor speed and the elevon reversal speed. Again, since B is typically very small, Eqs. (12) and (13) may be simply approximated as:

$$\left.\frac{\phi}{\delta}\right|_{SS} \cong -A_4\,\frac{c_{l\delta}}{c_{l\alpha}}\,\frac{\bar{\Omega}^2}{\bar{\Omega}_R^2} \tag{14}$$

$$\left.\frac{\beta}{\delta}\right|_{SS} \cong \frac{\gamma}{8}\,A_4\,\frac{c_{l\delta}}{c_{l\alpha}}\,\frac{\bar{\Omega}^2}{\left(\bar{\omega}_\beta^2 + \bar{\Omega}^2\right)}\left[1 - \frac{\bar{\Omega}^2}{\bar{\Omega}_R^2}\right] \tag{15}$$

In Eq. (15), the first term dominates at low rotor speed and flap bending response increases with $\bar{\Omega}^2$; at higher rotor speeds the second term dominates and produces elevon reversal when $\bar{\Omega} = \bar{\Omega}_R$.

Note that the flap bending and torsion *moment* responses of the rigid blade model are simply related to the flap and torsion *motion* response in Eqs. (8) - (15) by multiplying the deflections by the spring stiffnesses:

$$M_\phi/\delta = K_\phi\,(\phi/\delta) \text{ and } M_\beta/\delta = K_\beta\,(\beta/\delta) \qquad (16)$$

4.2 Elastic Blade 2GCHAS Model

A relatively complete model of the elastic rotor blade was modeled with the 2GCHAS code. This comprehensive analysis, Ref. 14, provides detailed finite element models of complex rotorcraft configurations including numerous optional representations for structures, aerodynamics, controls, as well as a variety of solution algorithms. For the present purposes only a few of these capabilities were required. The cantilevered blade was modeled with twelve finite elements, primarily nonlinear beam elements, to represent the flapwise bending, chordwise bending, and elastic torsion deflections. These elements represented the hub, the inboard flexure region, a transition region, several constant property inboard and outboard blade sections, the active section containing the actuators and elevon, and a tip mass section. Measured or estimated blade properties, including geometry, mass, and stiffness, were assigned to each of these finite elements. Inertial excitation caused by the elevon actuator deflection was included in the model but results for these effects are not included herein. Two percent structural damping was assumed.

The aerodynamic modeling included a distribution of nine spanwise aero segments with airloads based on linear aerodynamics. For the limited present purpose of addressing blade frequency response characteristics, rather than prediction of rotor loads in forward flight, a constant uniform inflow was used for the rotor wake. Unsteady aerodynamic effects were provided by linear, incompressible, Theodorsen thin airfoil theory (implicit 2-D shed wake) to model airfoil lift and moment due to elevon deflection including the variation of the Theodorsen function, $C(k)$, with reduced frequency. This approach is considered suitable for the preliminary calculations included herein. Future analysis may include more refined 3-D unsteady dynamic wake effects available in 2GCHAS to represent aerodynamic coupling between blades.

Solutions were obtained in hover and forward flight conditions by generating time domain responses for harmonic excitation of the elevon at discrete frequencies, post-processed to yield amplitude and phase of the flap bending and torsion moment response. The output amplitude results were normalized by elevon input to provide the FRF magnitudes.

5. INVESTIGATION OF ELEVON RESPONSE CHARACTERISTICS IN HOVER

In this section the unique characteristics of on-blade elevon response that were encountered during the hover experiments and described in section 3 will be investigated using the analytical models developed above. Quasi-steady response and elevon reversal will be studied with both analytical models and comparisons with the quasi-steady test data; low frequency dynamic response will be investigated with the rigid blade model; and the effects of torsion stiffness variations on elevon effectiveness will be investigated with the elastic blade model.

5.1 Quasi-Steady Blade Response and Elevon Reversal in Hover

The analytical models will now be compared with the quasi-steady experimental data for the torsion and flap bending moment response in hover. These results will also address elevon reversal characteristics. Since the quasi-steady measurements were made with a low frequency elevon excitation of 5 Hz, the analytical results will include this excitation frequency as well. The 5 Hz excitation is important for the flap bending moment response (since the first flap bending mode frequency is close to 5 Hz at 200 RPM) but it has a negligible effect on the torsion moment compared to the zero frequency result.

Before the results are presented, the values used for the elevon lift and moment coefficients $c_{l\delta}$ and $c_{m\delta}$ deserve some explanation. Because of the low Reynolds numbers of the experiments, the elevon coefficients would be expected to be substantially less than values based on classical thin airfoil theory. As discussed in Ref. 12, there is very little experimental airfoil elevon data available for low Reynolds numbers and, therefore, the coefficients used herein were inferred from the quasi-steady torsion and flap bending moment measurements. The elevon moment coefficient $c_{m\delta}$ was determined by fitting the torsion moment data to Eq. (12). Using this value, the elevon lift coefficient $c_{l\delta}$ was then determined by fitting the flap bending data to Eq. (13). A similar process was used to determine adjustment factors for the Theodorsen theory

elevon lift and moment in the elastic blade model. The results of this curve fitting procedure are summarized as follows. For the rigid blade 2-DOF model, $c_{l\delta}$ and $c_{m\delta}$ were taken to be 0.2525 and 1.13 per rad (45.9% and 45% of 0.55 and 2.51, the ideal thin-airfoil theory values for a 10% chord flap), respectively. For the elastic blade 2GCHAS model, the elevon unsteady aerodynamic lift and pitch moment were reduced to 45% and 35% of the 2-D Theodorsen theory values for lift and pitch moment, respectively.

With the elevon aerodynamic coefficients corrected for Reynolds number in this fashion, the predicted variations of torsion and flap bending moments with rotor speed agree well with the measured data. These results will be shown in the next two figures.

Torsion moment comparisons are given in Fig. 10. The rigid and elastic blade analytical results are essentially identical and both reflect the fact that the elevon-induced aerodynamic pitch moment increases with the square of the rotor speed, in accordance with Eq. (14).

The analytical and experimental flap bending moments are compared in Fig. 11. The elevon reversal behavior is clearly evident in this figure. At low rotor speeds, the flap bending moment increases with the square of the rotor speed, Eq. (15), due to the elevon lift ($c_{l\delta}\ \delta$) effect. As rotor speed increases, the elevon aero moment produces a nose down elastic twist that progressively reduces the flap bending moment due to the torsion lift effect ($c_{l\alpha}\ \phi$). For higher rotor speeds the flap bending moment becomes negative (beyond elevon reversal). In Fig. 11, the two analytical models yield similar values for the elevon reversal speed. The elastic blade flap bending moment results agree well with experiment while the rigid blade results are less satisfactory and under predict flap bending moment at the higher rotor speeds. Dynamic effects for the relatively low 5 Hz excitation frequency are not negligible as noted above, and may be seen by comparing the rigid blade results for zero frequency with the rigid blade results for 5 Hz excitation. (Note that with 5 Hz elevon excitation the elastic blade bending moment does not quite vanish at the elevon reversal speed before increasing for higher rotor speeds. This is because the magnitude (absolute value) of the bending moment is plotted in the figure and a small out-of-phase component is present at the elevon reversal speed.)

5.2 Low Frequency Dynamic Response Characteristics in Hover - Rigid Blade Model

To provide insight about basic dynamic phenomena relating torsion, flap bending, and elevon reversal, the 2-DOF rigid blade model will be used to examine the magnitude and phase of frequency response functions calculated from Eq. (7). The experimental model will be used as the baseline configuration with the following physical property values: Ω_o = 760 RPM, γ = 6.0, $\omega_\beta = 0.293\Omega_o$, $\omega_\phi = 4.34\Omega_o$, $c_{mq} = \pi/8$, $c_{l\alpha} = 2\pi$, I/I_ϕ = 0.000921, $r_i = 0.698R$, $r_o = 0.802R$, c = $0.0755R$, and η_ϕ = 0.025. The elevon aerodynamic coefficient derivatives are assigned the same values discussed above. The corresponding elevon reversal speed is Ω_R = 771 RPM from Eq. (11). Results are presented for the three rotor speeds used for the hover experimental investigations, 200, 425, and 760 RPM, as well as additional values to more fully explore conditions below and above elevon reversal.

The torsion moment FRF magnitude and phase given in Figs. 12 and 13 are reviewed first. The torsion mode is uncoupled from the flap mode and the results reflect elementary behavior of a 1-DOF system. The torsion amplitude at resonance is roughly five times the steady-state value, consistent with the experimental results at 760 RPM. Also note in Fig. 13 that the phase is -180 deg at zero frequency corresponding to the negative torsion deflection (positive nose up) produced by positive elevon deflections (trailing edge down). In the high frequency limit, the phase approaches -360 deg.

The corresponding magnitude of the flap bending FRF is given in Fig. 14a for a number of rotor speeds. The two peaks in the response correspond to the first flap bending and torsion natural frequencies. The behavior of the flap bending mode is most interesting and provides much insight about the results observed during the model rotor experiments. At low rotor speeds, 100 to 200 RPM, the flap bending mode resonant response is present. For further increases in rotor speed from 425 RPM to 800 RPM both the static response at $\omega = 0$ and the resonant peak decrease dramatically. The former effect is simply elevon reversal as defined by Eq. (11), while the latter may be thought of as the influence of elevon reversal on the flap bending frequency response at low frequencies. At the elevon reversal speed, just below 800 RPM, the static flap bending moment vanishes. Further increases in rotor speed restore

both the static response and the resonant peak response.

By expanding the lower left portion of Fig. 14a it is easier to observe the effects of combinations of rotor speed and frequency in the elevon reversal region. Figure 14b traces the locus of the flap bending mode peak resonant response and it is easy to see the abrupt collapse of the flap mode resonant response peak simultaneous with the static bending response vanishing as elevon reversal is approached, followed by the increase in magnitude of static response and the resonant peak beyond elevon reversal.

Returning to Fig. 14a, the flap bending moment response peak near the torsion natural frequency is driven by resonant torsion motion. Here the uncoupled torsion mode is essentially driving the flap bending mode open loop, and since the torsion resonant frequency is well above the flap mode natural frequency, the dynamic response is relatively straightforward. Interestingly, there appears to be little influence of elevon reversal phenomena in this elevon frequency range as evident from the monotonic increase in bending moment response with rotor speed. That is, there is no reduction in response as rotor speed passes through the elevon reversal speed as was the case for frequencies near the flap bending mode. The explanation for this behavior can be related to the effects of rotor speed and excitation frequency on the relative influence of the elevon lift effect and the torsion lift effect that will be discussed below.

The corresponding phase characteristics of the flap bending FRF are presented in Fig. 15. For all rotor speeds below elevon reversal, $\Omega < \Omega_R$, (elevon lift greater than torsion lift), the phase is zero at $\omega = 0$ since positive elevon deflection (trailing edge down) produces upward lift and positive blade flapping motion. As the frequency increases to values exceeding the flap natural frequency, a phase shift approaching -180 deg occurs in the conventional manner for a 1-DOF second order system. As the excitation frequency approaches ω_ϕ, varying amplitude and phase of the combined elevon and torsion lift (due to torsion dynamics) reduce the phase lag. When the frequency exceeds the torsion natural frequency the phase lag recurs until, in the limit, it reaches -180 deg.

For post-reversal rotor speeds in Fig. 15, the initial phase is 180 deg at $\omega = 0$ and decreases continuously in two 180 deg increments as the excitation frequency successively exceeds the flap and torsion natural frequencies. The most remarkable behavior occurs at low frequencies for rotor speeds in the vicinity of elevon reversal. In extreme cases, just below reversal speed, a strong phase lead occurs at low excitation frequencies.

Based on these rigid blade model results, some conclusions about elevon reversal and bending-torsion interactions may be made. These explanations may be understood in terms of the elevon lift effect and the torsion lift effect discussed in the introduction. First, the elevon reversal phenomena is principally important at low frequencies, where low is meant with respect to the torsion natural frequency, ω_ϕ. This is because elevon reversal results mainly from addition or subtraction of torsion lift from elevon lift when torsion motion is nearly in or out of phase with elevon motion (0 or 180 deg). Whether the rotor speed is below or above the elevon reversal speed determines whether the elevon lift effect ($\Omega < \Omega_R$) or the torsion effect ($\Omega > \Omega_R$) dominates.

For higher frequencies closer to ω_ϕ, the phase lag in torsion lift (90 deg when $\omega = \omega_\phi$) precludes a cancellation of the elevon lift by the torsion lift since the lift components combine vectorially (viewed in the complex plane). At torsion resonance, $\omega = \omega_\phi$, the torsion lift is several times the static torsion lift and the torsion lift effect dominates the combined torsion and elevon lift. At these frequencies it is clear that operation at the elevon reversal speed would have little influence on the response. Finally, for higher frequencies ($\omega > \omega_\phi$), where the torsion phase lag approaches 180 deg, the elevon and torsion lift will be in phase, (irrespective of rotor speed), but the torsion motion amplitude vanishes for large ω, so the elevon lift effect will dominate the combined lift.

These same principles may be used to understand the relative importance of the elevon lift effect and torsion effect for the higher flap bending modes in the case of an elastic blade by taking into account the relationship of the torsion mode frequency relative to the frequency of the flap bending mode of interest as well as mode shape effects.

The results of this section imply that elevon reversal characteristics will not be of primary importance for elevon vibratory load effectiveness at the principal N/rev frequencies of three and above since the torsion frequency of conventional rotors typically is in this frequency range as well. As explained above, the elevon lift and torsion lift components will combine vectorially rather than cancel at the elevon reversal speed and thus minimize the effect of elevon reversal.

5.3 Effects of Torsion Stiffness on Dynamic Response in Hover - Elastic Blade Model

The flap bending response and elevon reversal characteristics were investigated in the previous section by varying rotor speed, mainly because this was the parameter used in the experiments. It is useful, however, to do parametric studies using variables most relevant to full scale design practice. Therefore, a brief examination of blade torsional rigidity will be conducted using the elastic blade model to extend some of the results of the previous rigid blade study. Elevon reversal and torsion mode interactions with the 2nd and 3rd flap bending modes will be examined by varying torsional rigidity (GJ). Earlier investigations (Refs. 5 - 8) have indicated that the torsion frequency significantly influences the effectiveness of on-blade controls for vibration reduction.

The elastic blade 2GCHAS analytical results are shown for both torsion and flap bending moments in Figs. 16 and 17 for the 760 RPM rotor speed. In addition to the baseline torsional rigidity, ω_ϕ = 4.5/rev, three additional values are included to provide blade torsion natural frequencies of 2.5, 3.5, and 5.5/rev to bracket the nominal second flap bending mode natural frequency of 3.4/rev. Torsion frequency changes were made by varying torsional rigidity, GJ, with torsion inertia held constant.

It is of interest to first compare the baseline elastic blade response with the rigid blade 760 RPM baseline; the torsion moments (Figs. 12 and 16) are similar but flap bending moment responses (Figs. 14a and 17) differ significantly. The responses of the elastic blade 2nd and 3rd bending modes are now prominent while the bending moment amplification at the torsion natural frequency is not as prominent as it was for the rigid blade result. Interestingly, however, the elastic blade case with the lowest torsion frequency, ω_ϕ = 2.5/rev, does show prominent flap bending moment response at the torsion mode frequency.

Considering now all four configurations, the torsion moment response amplitude in Fig. 16 shows peak resonant response increasing with torsion frequency. The flap bending moment responses in Fig. 17 show very strong influence of torsion frequency, particularly the increase in response for the lower torsion frequency configurations. These effects may be partly explained by increased coupling of the torsion mode with the 2nd flap mode (frequency coalescence), but mainly from increased torsion motion resulting from decreased torsion stiffness reacting a constant elevon aero moment ($\phi \sim M_{aero}/GJ$). It may also be noted that the elevon reversal speed decreases with torsion frequency, Eq. (11), so that the two lowest torsion frequency configurations in Fig. 16 are operating beyond elevon reversal at the nominal 760 RPM rotor speed. This also explains the re-emergence of the first flap bending mode response for the lower torsion frequency configurations.

For practical application to elevon blade control, the result of most interest is the ability of the elevon to induce large flap bending response at the N/rev frequencies 3/4/5/rev, etc., where the principal vibratory airloads excitations occur. A clear picture of the elevon effectiveness at these frequencies may be obtained by cross-plotting the results in Fig. 17 as a function of the uncoupled torsional natural frequency. Figure 18 shows elevon effectiveness at the N/rev frequencies and shows that optimum effectiveness occurs when the torsion frequency is near N/rev for each harmonic, a not surprising result. Given that rotor harmonic airload excitations generally decrease with harmonic number it is logical to conclude that maximizing the elevon effectiveness at the important 3/rev harmonic frequency would be a desirable objective. This would seem to be generally consistent with Refs. 5 - 8, that found lower torsion frequencies to be beneficial.

Although elevon effectiveness for the important 3/rev flap bending response improved with a reduction in elevon reversal speed, it is clear that this is a coincidental effect and that the principal cause is the reduction in torsional stiffness. Therefore, it may be concluded that elevon reversal will be of much less importance than structural dynamics considerations in determining elevon control effectiveness at the 3/4/5/rev frequencies primarily responsible for both vibratory blade loads and rotor vibratory loads transmitted to the vehicle

6. HOVER DYNAMIC RESPONSE - ANALYSIS AND EXPERIMENT COMPARISONS

In this section, the experimentally measured frequency responses for the hover condition at 200, 425, and 760 RPM (discussed earlier, Figs. 4-5) will be compared with analytical predictions from the 2GCHAS elastic blade model and the rigid blade model. The purpose is to use the comprehensive analysis to investigate the principal experimental phenomena rather than to conduct a rigorous evaluation of the accuracy of the analysis. The latter objective would require more precise evaluation of the model rotor blade physical

properties than was appropriate for this exploratory investigation. Both the blade root bending and torsion moments will be examined below.

Analytical results for magnitude and phase of the torsion moment frequency response are compared with the experimental data in Figs. 19 and 20a-b respectively. Agreement of response magnitude is generally good at low frequencies and for the peak response at the torsion natural frequency for 760 RPM for both the elastic and rigid blade models. The results are less satisfactory for the peak responses at 425 and 200 RPM and at the higher frequencies for all three rotor speeds. At the higher frequencies, the experimental results substantially exceed the analysis.

The phase of the torsion moment response shown in Fig. 20a-b indicates qualitative similarity between the 2GCHAS and experimental results except at the higher frequencies, where differences up to 90 deg are observed. This may be related to the under prediction of the response magnitude at high frequencies noted above. The effects of rotor speed on phase are small but the analysis generally reflects these trends.

Comparative results for the magnitude of the flap bending moment response are shown in Fig. 21a-c for each of the three rotor speeds. Note that different ordinate scales are used for each rotor speed. The principal features of the experimental results are reproduced in the analytical predictions for all three rotor speeds. At low frequencies, the effects of elevon reversal are clearly evident as rotor speed increases to approach reversal at 760 RPM. The differences are mainly in the amplitude of the resonant response peaks at the bending natural frequencies (particularly the third flap bending mode), and the differences in the apparent natural frequencies of the second and third flap bending mode natural frequencies (particularly for 760 RPM). The differences in natural frequencies can be attributed to the lack of fine tuning of the blade stiffness and mass properties used for the analytical predictions. An interesting result is that the elastic blade predictions, by showing the small but unmistakeable influence of the torsion mode at 425 RPM and 760 RPM, corroborate evidence of the torsion mode that is barely visible in the experimental data.

Figure 22 shows more detailed comparisons of flap bending moment responses for the low frequency range, now plotted on the same scale, and including results from the 2-DOF rigid blade model. The experimental results are especially interesting in this frequency range because of the interaction of the first flap bending mode and elevon reversal characteristics studied earlier using the rigid blade 2-DOF analysis. Comparisons of both analytical models and experimental data for the three rotor speeds show instances of both good and poor correlation. Although the principal features are reasonably well represented, in some areas the trends are not well captured.

The blade root bending moment phase results predicted by the elastic blade model are compared with the experimental data in Figs. 23a and 23b by using separate plots for the two sets of results. There are remarkable overall similarities, particularly the initial phase of about 360 deg at zero frequency for 760 RPM, although, quantitatively, there is a difference in phase of about 90 deg at the maximum frequency.

It is of interest to compare the analytical flap bending moment phase results of the rigid blade model in Fig. 15 with the elastic blade model in Fig. 23a. The phase responses show distinct similarities, despite the differences associated with the elastic blade's two additional degrees-of-freedom. One difference is more difficult to reconcile: at 760 RPM the phase of the elastic blade response begins at 360 deg for zero frequency, even though 760 RPM is slightly below the elevon reversal speed. In the case of the rigid blade model, it was necessary to exceed the elevon reversal speed before the initial phase shifted from zero to 180 deg.

In concluding, comparisons of the analysis with experimental data show that the 2GCHAS model qualitatively captures the essential physical phenomena of elevon reversal, the higher elastic bending and torsion mode interaction, and the basic phase characteristics. Lack of quantitative acacuracy can be attributed to several possible sources including nonlinear aerodynamics, 3-D unsteady aerodynamics and wake effects, inertial excitations of the elevon actuator masses, structural damping, and possible physical variations due to the small scale of the model blades and observed as differences in the data measured on each of the two blades.

7. FORWARD FLIGHT DYNAMIC RESPONSE

7.1 Experimental Results (FRFs)

Dynamic response characteristics of the rotor in forward flight were determined in Ref. 13 with the same frequency sweep elevon excitation and CIFER® post-processing techniques used for the hover experiments. The torsion and flap bending moment FRF magnitudes for a range of advance ratio up to 0.3 are presented in Figs. 24 and 25 for 760 RPM at a collective pitch of 4 deg. It was possible to attain advance ratios up to 0.6 by reducing collective pitch to zero and rotor speed to 450 RPM; these results are presented in Figs. 26 and 27. Although the forward flight FRFs have lower coherence than the hover results, the principal trends with advance ratio are evident. The 760 RPM results show the effects of low coherence in the form of spikes in the FRF at the N/rev harmonic frequencies.

The torsion moment FRFs in Figs. 24 and 26 show only a relatively small reduction in amplitude with advance ratio. Also included are the discrete data points for the elevon-induced moment response derivatives determined from discrete frequency excitation phase sweeps discussed in section 3.2. Qualitatively the two results are very similar; some quantitative differences are evident at 760 RPM.

The flap bending moment responses in Figs. 25 and 27 generally show two effects of advance ratio. First, the largest effect of advance ratio appears in the response at low frequencies (0 - 20 Hz). At 450 RPM, where the rotor is below the elevon reversal speed in hover, increasing advance ratio increases the mean dynamic pressure similar to an increase in RPM. This causes the rotor to more closely approach elevon reversal and reduces flap bending response for the low frequency range. At 760 RPM, where the rotor is already close to elevon reversal in hover, increasing advance ratio causes elevon reversal to be exceeded, thus increasing FRF magnitude with advance ratio.

The second effect of advance ratio on the flap bending moment is to alter FRF peak responses at the torsion, second flap and third flap bending mode resonant frequencies, generally reducing the magnitude of the peak response, suggesting an increase in effective modal damping. It must be noted however, that these effects are not very large and therefore it is difficult to make conclusions about advance ratio trends.

The discrete frequency excitation phase sweep results for the elevon-induced moment response derivatives presented in section 3.2 (Figs. 8 and 9) are also included in Figs. 25 and 27 for flap bending moment at the N/rev harmonic frequencies. In general, they agree well with the continuous frequency FRFs except, perhaps, the 1/4/5/rev responses at 760 RPM.

Comparison of the continuous FRFs and discrete elevon-induced moment response derivatives in forward flight for the two different rotor speeds provides additional insights about the effect of structural dynamics on elevon effectiveness (as noted earlier in section 3.2). For example, the low elevon effectiveness for the 2/3/4/rev frequencies at 450 RPM compared to 760 RPM can be seen to be associated with very low dynamic response between the 1st and 2nd flap bending mode resonant response peaks, including an apparent antiresonance at 3/rev.

7.2 Comparisons with 2GCHAS Forward Flight Predictions

The torsion and flap bending moment FRFs were calculated with the 2GCHAS elastic blade model at 760 RPM for a range of forward flight advance ratios (0 - 0.4) and the results are presented in Figs. 28 and 29.

Before discussing the results, a few explanatory comments about the analysis process are in order. Since the equations contain periodic coefficients due to the azimuthal variation of blade velocity in forward flight, the frequency response is not independent of the phase of the excitation (with respect to azimuth), as in hover. The FRFs were therefore calculated by 2GCHAS using discrete frequency (ω) elevon cosine and sine excitations to compute the flap bending moment response time history in the rotating system. Following convergence to a steady-state periodic response, harmonic analysis gave the amplitude and phase of the component of response at the excitation frequency (side-band components at the ω +/- NΩ frequencies were also determined, but need not be addressed here).

The resulting FRF amplitude and phase for the cosine and sine excitations were found to be equal *except* for frequencies identically equal to multiples and half-multiples of the rotor speed (N and N/2 per rev). Furthermore the cosine and sine responses at these frequencies are not continuous with the remainder of the FRF computed at

frequencies not equal to multiples of N/2 and N. These additional discrete values corresponding to cosine and sine excitations are included in Fig. 29 except where the effect is small - for bending moment above 2.5/rev and for the torsion moment at all frequencies.

This apparently unusual result may be explained as follows. The 1/rev frequency case is easily understood, since cosine and sine elevon inputs are analogous to conventional lateral and longitudinal cyclic pitch. It is well understood that these inputs produce different values of flapping response amplitude and phase in forward flight. This familiar behavior occurs because (when $\omega = 1/\text{rev}$) both the excitation and response are "phase-locked" to the periodic azimuthal variations in velocity. Viewed another way, the blade flap-bending response appears as a stationary tilt of the rotor disc as viewed in the fixed system. For frequencies not identically equal to integer and half-integer frequencies, the mathematics of periodic systems does not permit this phase-lock to occur and the differences between cosine and sine excitation average out over time. In the fixed system the rotor disc tilt is non-stationary and precesses or "wobbles" in time for these non-integer frequencies. In the case of integer frequencies greater than one, the rotor disc is stationary but warped and for $\omega = N/2$, two stationary rotor discs appear, i.e., split tip path planes. Combinations of warping and multiple tip path planes occur for half-integer frequencies above 1/rev (1.5, 2.5, ...).

Returning to the analytical results, the torsion moment response in Fig. 28 shows small increases in peak response with advance ratio, as might be expected from increased average dynamic pressure with advance ratio. This result contrasts with the advance ratio trend of the experimental torsion results in Fig. 24 as discussed above. The source of small discontinuities in the analytical results near 1/rev and 2/rev are not known but may be due to numerical anomalies from post-processing the calculated time history responses.

The analytical flap bending moment results in Fig. 29 may be compared with the experimental results in Fig. 25. The general trends at low frequency are reflected in the analytical results, however, the effect of advance ratio on the peak responses at the 2nd and 3rd flap bending moment is opposite the trend for the experimental results.

A clearer view of the flap bending moment analytical and experimental results at low frequencies, in the region of elevon reversal, is given by comparing Figs. 30a and 30b, where results from the previous figures are expanded. Here the analysis over predicts the aerodynamic effects of advance ratio.

It may be noted that multiple responses at integer or half-integer frequencies are not evident in the forward flight experimental FRFs. In the case of the frequency sweep FRFs, the nature of the transient excitation would likely average out the two distinct responses unless the excitation were properly tailored. In the case of discrete phase sweep excitations, the FRF identification process was based on the assumption that the magnitude of the elevon induced moment was independent of excitation phase and therefore can be expected to represent an average of the two values.

To summarize the discussion it may be concluded that the principal effect of advance ratio is now understood for this rotor, while other effects remain to be explained. The primary advance ratio effect evident in the experimental data and corroborated by the 2GCHAS results is the low frequency elevon reversal behavior that is strongly affected by advance ratio. Specifically, both the experiment and 2GCHAS show that an increase in advance ratio can push the rotor towards and beyond elevon reversal (Figs. 25, 27, and 29), depending on the particular combination of rotor speed and advance ratio. A secondary and generally smaller advance ratio effect is a change in the amount of resonant amplification exhibited at the second and third flap bending modes and the first torsion mode. Unfortunately, this advance ratio effect is not well understood as the experimental data and the 2GCHAS results do not exhibit the same trends. Additional analysis and/or experimentation should be performed to resolve these unanswered questions.

8. CONCLUDING REMARKS

1. As first reported in Ref. 13, forward flight testing of a model scale rotor system successfully demonstrated the capability of on-blade elevon controls to significantly reduce vibratory loads in forward flight.

2. Comparison of the experimental data with both analytical models indicates that elevon aerodynamic coefficients ($c_{m\delta}$ and $c_{l\delta}$) were about half the level given by thin airfoil theory, indicating the importance of testing rotors with on-blade elevon controls at representative Reynolds numbers.

3. Analytical predictions for the elastic blade model successfully reproduced the principal physical characteristics observed in the experimental data including elevon reversal, FRF magitude and phase, and most of the effects of advance ratio.

4. A simplified analytical model was very helpful in clarifying and interpreting the unique effects of elevon reversal on rotor blade dynamic response and elevon effectiveness.

a. Elevon reversal (defined at $\omega = 0$) is strongly felt in the flap bending response at low (relative to the torsion mode) frequencies. Resonant response of the first flap mode is largely eliminated at the elevon reversal speed.

b. Elevon reversal is much less important for higher frequencies associated with control of blade vibratory loads.

5. For frequencies well below the torsion mode, the elevon lift effect is dominant below the reversal speed, while torsion lift dominates above the reversal speed. Near the torsion mode frequency, elevon reversal is not important and neither elevon or torsion lift is dominant. Well above the torsion mode, the elevon lift effect is dominant.

6. Parametric analysis of blade torsional stiffness using the elastic blade model showed that benefits to elevon vibratory load effectiveness improved with low torsion rigidity and for ω_ϕ close to the 2nd flap mode.

7. Advance ratio has only a small effect on flap bending and torsion moment FRFs except for low excitation frequencies and these effects can be understood in terms of elevon reversal behavior.

8. Calculation of elevon response in forward flight showed an unexpected result that the FRF magnitude is independent of elevon excitation phase except for frequencies equal to integer and half-integer multiples of rotor speed.

9. As concluded in Ref. 13, a complete evaluation of the practical effectiveness and suitability of active on-blade elevon controls for fuselage vibration reduction will require additional testing with more sophisticated rotor models, measurement of rotor hub vibratory loads, concurrent evaluation with analytical models, and inclusion of closed loop active control systems.

Acknowledgment

The authors wish to recognize the contribution of Dr. Hossein Saberi in helping to identify and explain the nature of the discontinuous analytical results for forward flight frequency response functions.

9. REFERENCES

1. Strehlow, H., and Rapp, H., "Smart Materials for Helicopter Rotor Active Control," Paper No. 5, *Presented at the AGARD/SMP Specialist's Meeting on Smart Structures for Aircraft and Spacecraft*, Lindau, Germany, October 5-7, 1992.

2. Chopra, I., "State-of-the-Art of Smart Structures and Integrated Systems," *SPIE Smart Structures and Materials Conference*, San Diego, CA, Feb 25-29, 1996.

3. Loewy, R.G., "Recent Developments in Smart Structures with Aeronautical Applications," *37th Israel Annual Conference on Aerospace Sciences*, Tel Aviv, Haifa, Israel, February 26-27, 1997.

4. Ormiston, R.A., "Can Smart Materials Make Helicopters Better?," *Presented at the Fourth Workshop on Dynamics and Aeroelastic Stability Modeling of Rotorcraft Systems*, College Park, Maryland, November 19-21, 1991.

5. Millott, T.A., and Friedmann, P.P., "Vibration Reduction in Helicopter Rotors Using an Active Control Surface Located on the Blade," AIAA-92-2451-CP, *Proceedings 33rd AIAA/ASME/ASCE/AHS/ASC Structures, Structural Dynamics, and Materials Conference*, Dallas, TX, April 13-15, 1992, pp 1975-1988.

6. Millott, T.A., and Friedmann, P.P., "Vibration Reduction in Helicopter Rotors Using an Actively Controlled Partial Span Trailing Edge Flap Located on the Blade," NASA CR 4611, June 1994.

7. Milgram, and Chopra, I., "Helicopter Vibration Reduction with Trailing Edge Flaps," *Proceedings of the American Helicopter Society Northeast Region Aeromechanics Specialists' Meeting*, Stratford, Connecticut, October, 1995.

8. Milgram, J., and Chopra, I., "Dynamics of an Actively Controlled Plain Trailing Edge Flap System for a Modern Bearingless Rotor," Proceedings of the 23rd European Rotorcraft Forum, Dresden, Germany, September 16-18, 1997.

9. Spangler, R.L., and Hall, S.R., "Piezoelectric Actuators for Helicopter Rotor Control," Paper No. 90-1076-CP, *Proceedings of the 31st Structures,*

Structural Dynamics and Materials Conference, Long Beach, California, April 2-4, 1990.

10. Walz, C., and Chopra, I., "Design and Testing of a Helicopter Rotor Model with Smart Trailing Edge Flaps," Paper No. 94-1767-CP, *Proceedings of the 35th Structures, Structural Dynamics and Materials Conference, Adaptive Structures Forum*, Hilton Head, South Carolina, April 18-20, 1994.

11. Ben-Zeev, O., and Chopra, I., "Advances in the Development of an Intelligent Helicopter Rotor Employing Smart Trailing-Edge Flaps," *Smart Materials & Structures*, Vol. 5, No. 1, 1996.

12. Fulton, M.V., and Ormiston, R.A., "Hover Testing of a Small-Scale Rotor with On-Blade Elevons," *Proceedings of the 53rd Annual Forum of the American Helicopter Society*, Virginia Beach, Virginia, April 29-May 1, 1997.

13. Fulton, M.V., and Ormiston, R.A., "Small-Scale Rotor Experiments with On-Blade Elevons to Reduce Blade Vibratory Loads in Forward Flight," *Proceedings of the 54th Annual Forum of the American Helicopter Society*, Washington, DC, May 20-22, 1998.

14. Rutkowski, M.J., Ruzicka, G.C., Ormiston, R.A., Saberi, H., and Jung, Y., "Comprehensive Aeromechanics Analysis of Complex Rotorcraft Using 2GCHAS," *Journal of the American Helicopter Society*, Vol. 40, (4), 1995.

15. Tischler, M.B., Cauffman, M.G., "Frequency-Response Method for Rotorcraft System Identification: Flight Applications to BO-105 Coupled Rotor/Fuselage Dynamics," *Journal of the American Helicopter Society*, Vol. 37, (3), 1992.

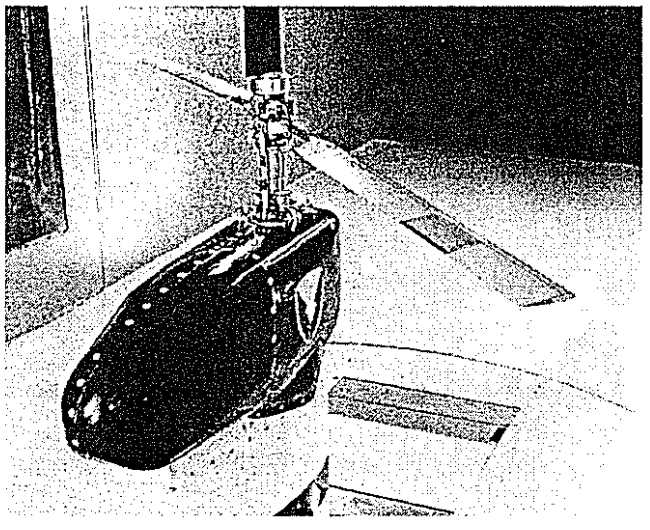

Fig. 1 Rotor Test Rig installed in the Army/NASA 7- by 10-Foot Wind Tunnel and two bladed 7.5-ft diameter model rotor showing 10% chord on-blade elevon located at 75% blade radius.

16. Tischler, M.B., Driscoll, J.T., Cauffman, M.G., and Freedman, C.J., "Study of Bearingless Main Rotor Dynamics from Frequency-Response Wind Tunnel Test Data," Presented at the American Helicopter Society Aeromechanics Specialists Conference, San Francisco, CA, January 19-21, 1994.

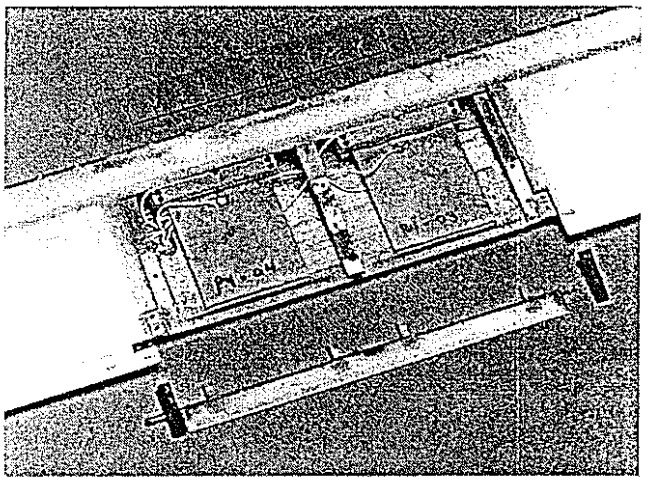

Fig. 2 Close-up of rotor blade (3.4-in chord) showing active section (spanning 12% of blade radius). Elevon and hinge pin bearing blocks disassembled and access panel removed showing two piezoceramic bimorph actuators cantilevered to blade spar.

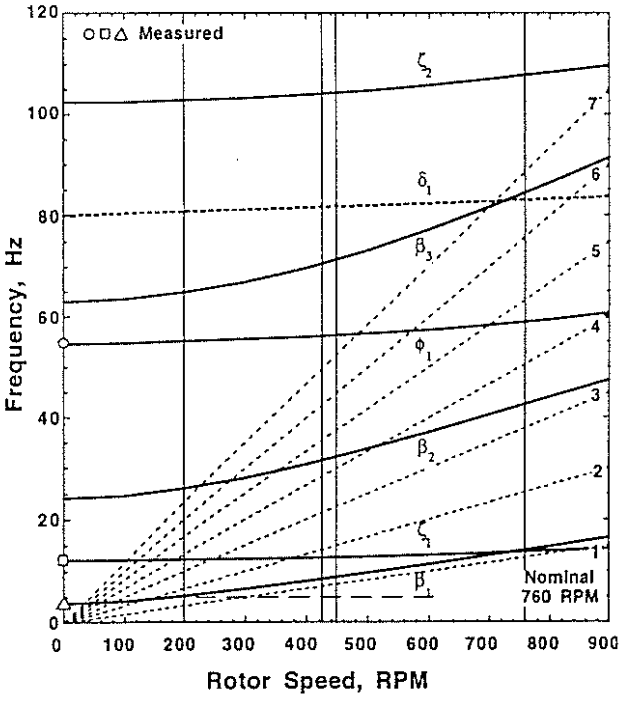

Fig. 3 Calculated rotor blade frequencies versus rotor speed in air at zero collective pitch. Notation for rotor blade mode identification: β - flap, ζ - lead-lag, ϕ - torsion, and δ - elevon angle.

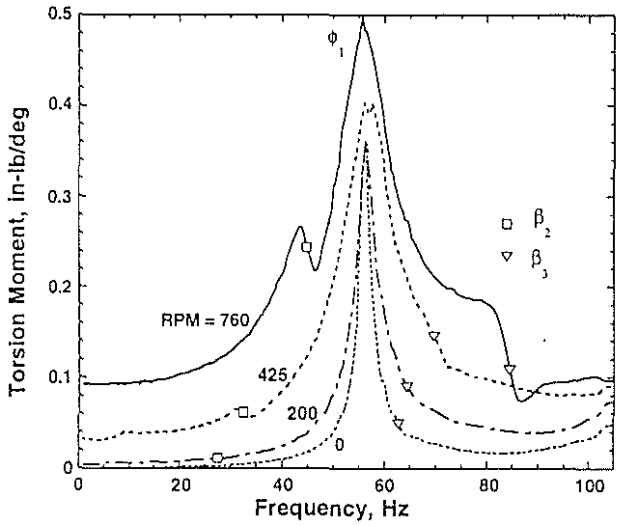

Fig. 4 Experimental blade root torsion moment frequency response in hover, $\theta_0 = 3.5$ deg.

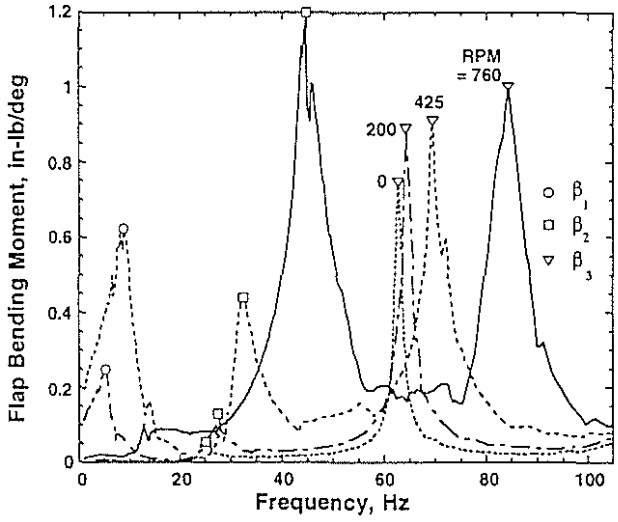

Fig. 5 Experimental blade root flap bending moment frequency response in hover, $\theta_0 = 3.5$ deg.

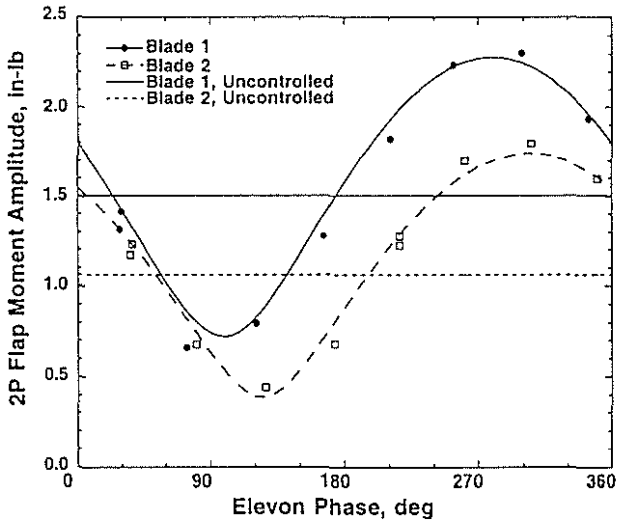

Fig. 6 Variation of 2/rev flap bending moment with elevon phase, 760 RPM, $\theta_0 = 4$ deg, $\mu = 0.2$.

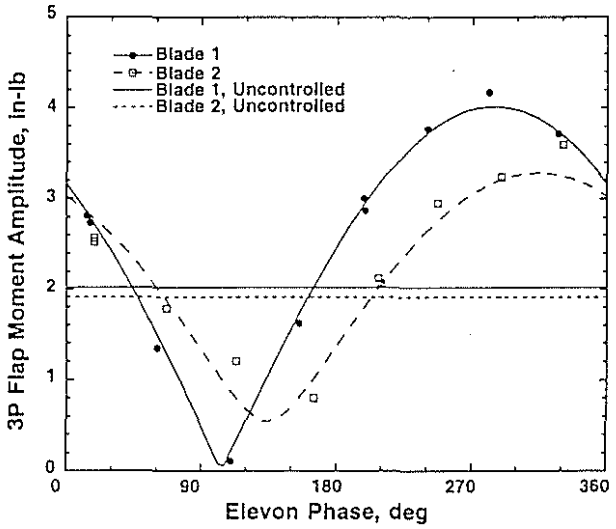

Fig. 7 Variation of 3/rev flap bending moment with elevon phase, 760 RPM, $\theta_0 = 4$ deg, $\mu = 0.2$.

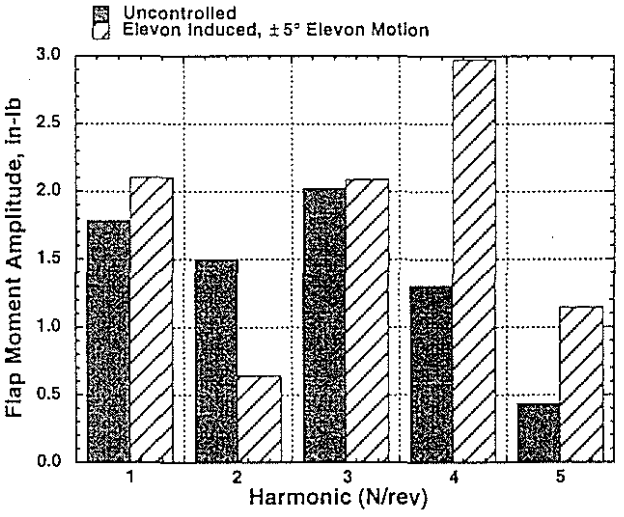

Fig. 8 Uncontrolled & elevon-induced flap bending moment, 760 RPM, $\theta_0 = 4$ deg, $\mu = 0.2$, blade 1.

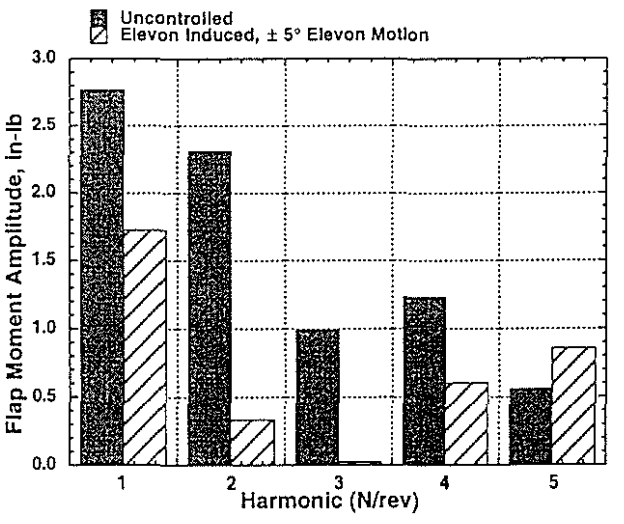

Fig. 9 Uncontrolled & elevon-induced flap bending moment, 450 RPM, $\theta_0 = 6.25$ deg, $\mu = 0.2$, blade 1.

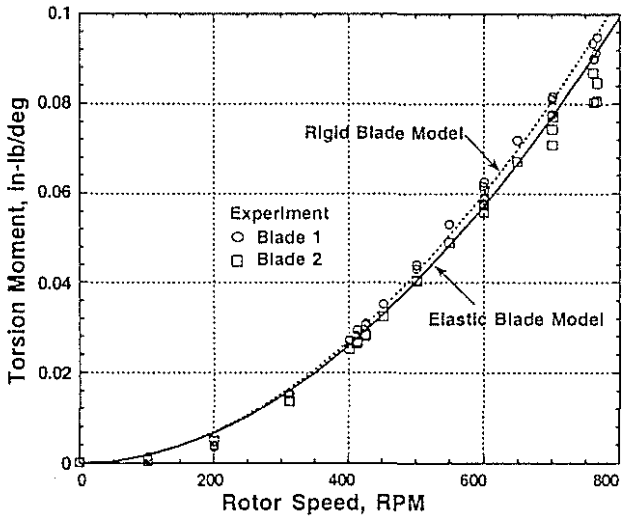

Fig. 10 Hover quasi-steady elevon torsion moment effectiveness versus rotor speed, 5 Hz, θ_0 = 3.5 deg.

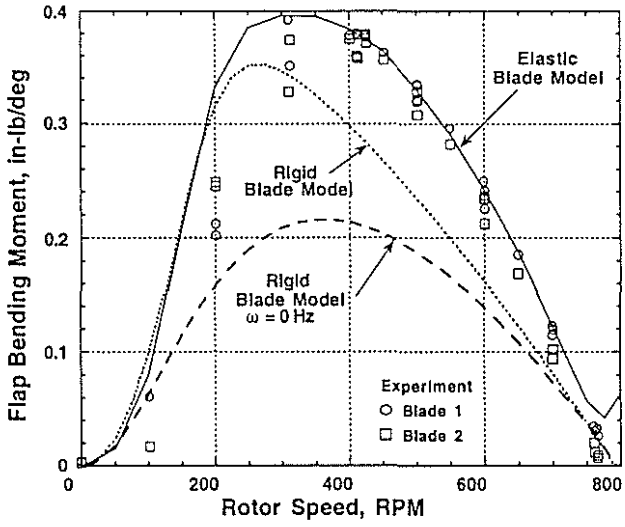

Fig. 11 Hover quasi-steady elevon flap bending moment effectiveness versus rotor speed, 5 Hz, θ_0 = 3.5 deg - "elevon reversal" effect.

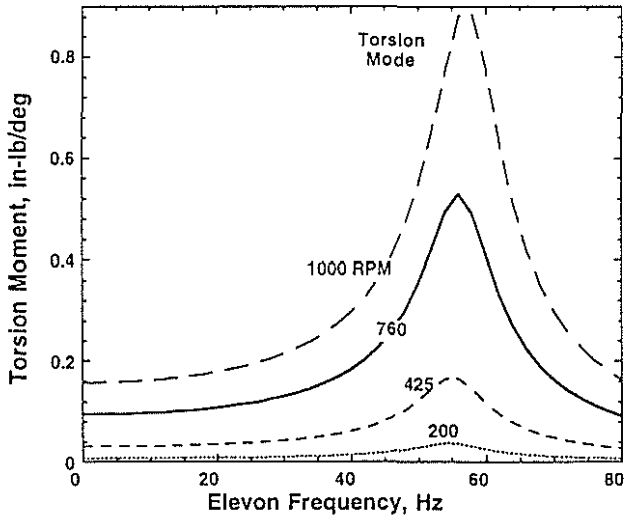

Fig. 12 Torsion moment frequency response magnitude in hover, rigid blade 2-DOF analysis.

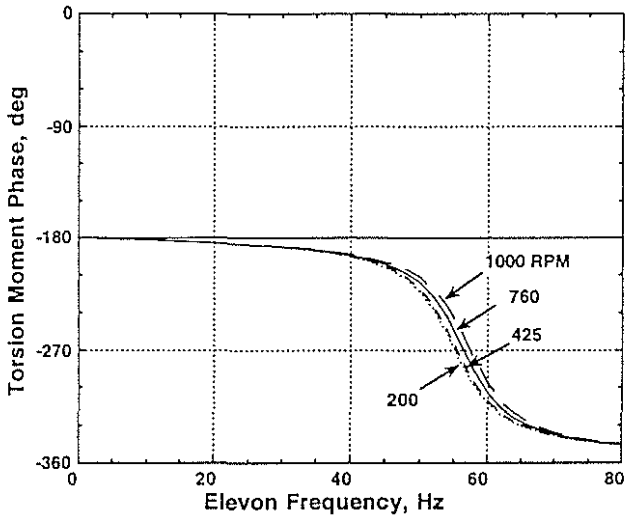

Fig. 13 Torsion moment frequency response phase in hover, rigid blade 2-DOF analysis.

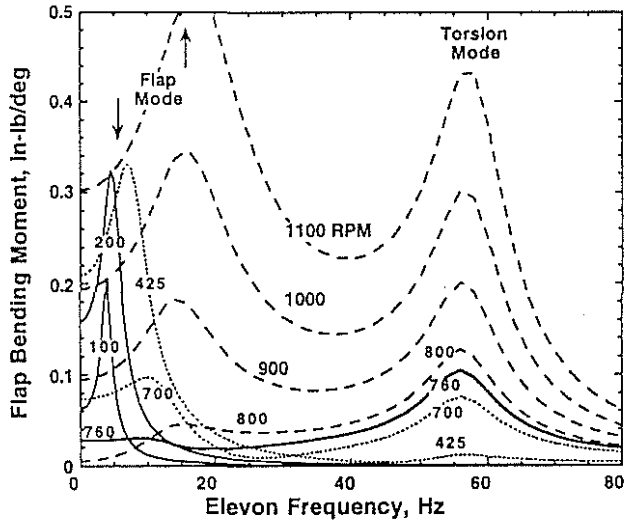

Fig. 14a Flap bending moment frequency response magnitude in hover, rigid blade 2-DOF analysis.

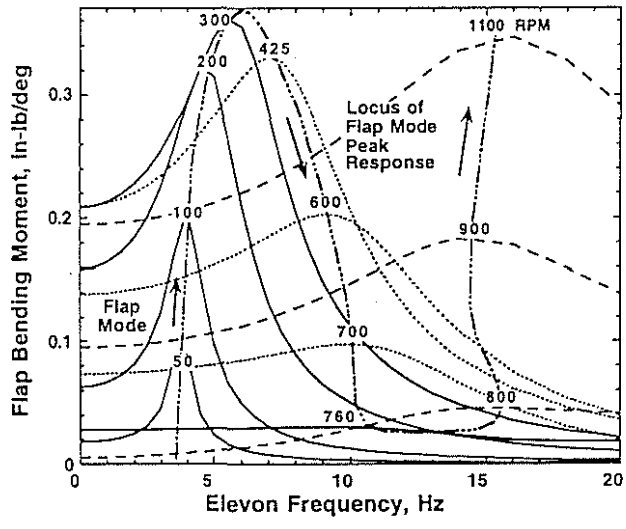

Fig. 14b Details of elevon reversal, Fig. 14a expanded for low frequency.

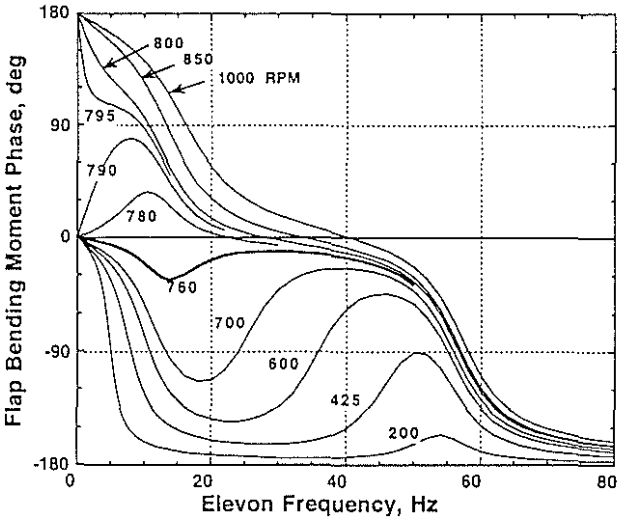

Fig. 15 Flap bending moment frequency response phase in hover, rigid blade 2-DOF analysis.

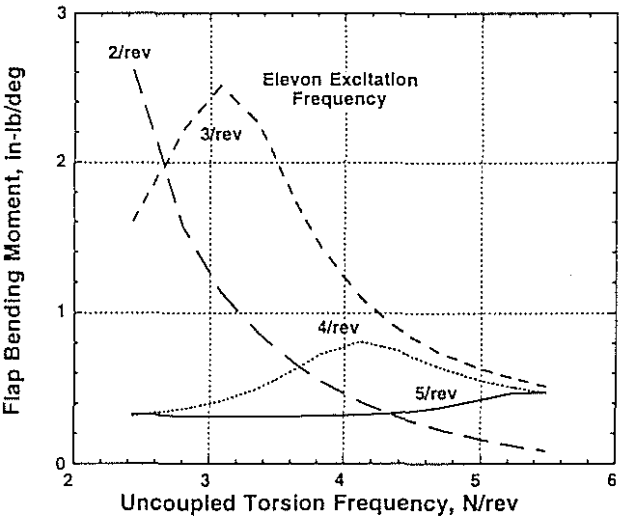

Fig. 18 Influence of torsion stiffness on elevon effectiveness for N/rev harmonics of flap bending moment, 760 RPM.

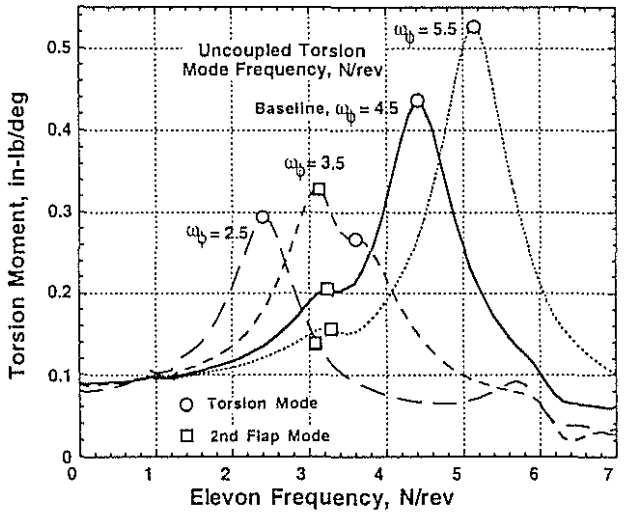

Fig. 16 Effect of torsion stiffness on torsion moment FRF magnitude, elastic blade analysis, 760 RPM.

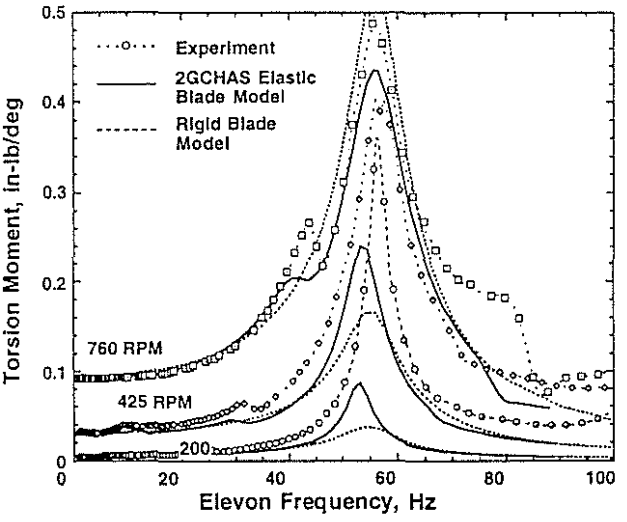

Fig. 19 Torsion moment FRF magnitude in hover, comparisons of analyses with experiment.

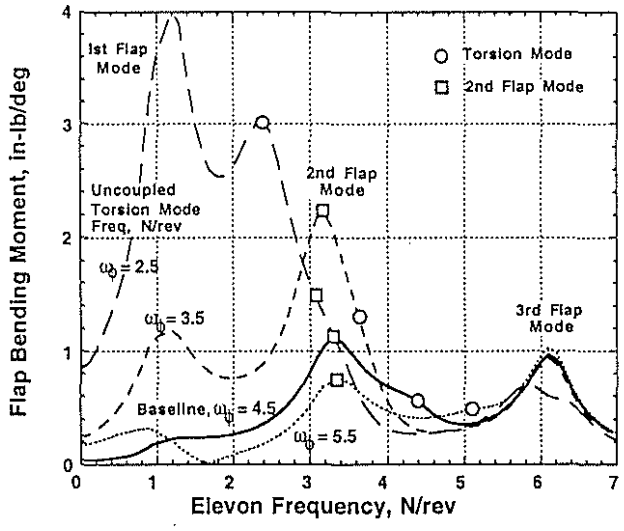

Fig. 17 Effect of varying torsion stiffness, GJ, on flap bending moment FRF magnitude, elastic blade analysis, 760 RPM.

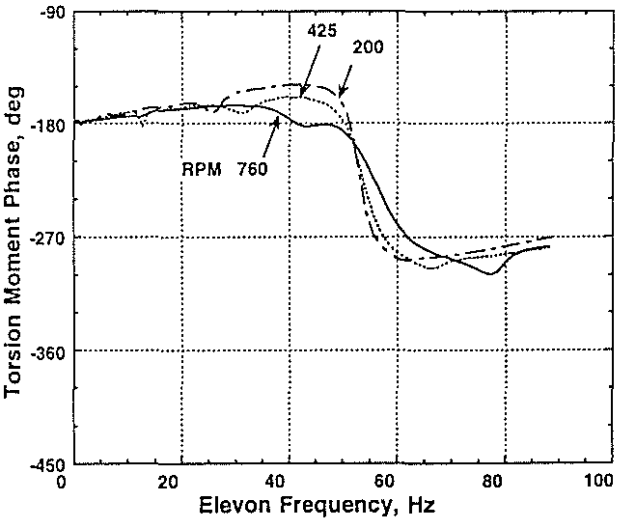

Fig. 20a Torsion moment FRF phase in hover from elastic blade analysis; compare with Fig. 20b.

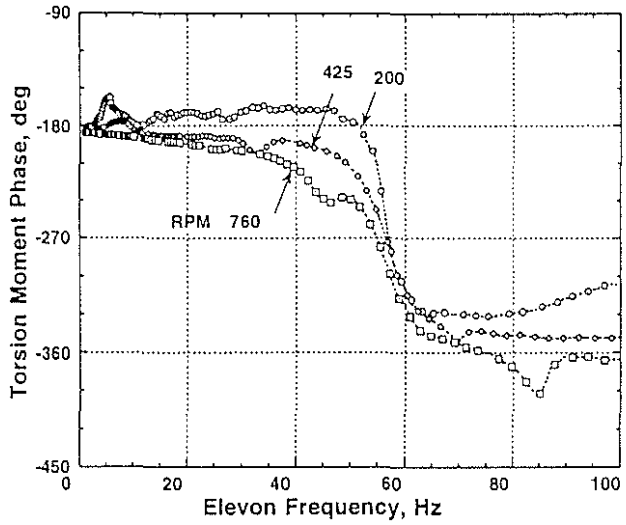

Fig. 20b Experimental torsion moment FRF phase in hover; compare with Fig. 20a.

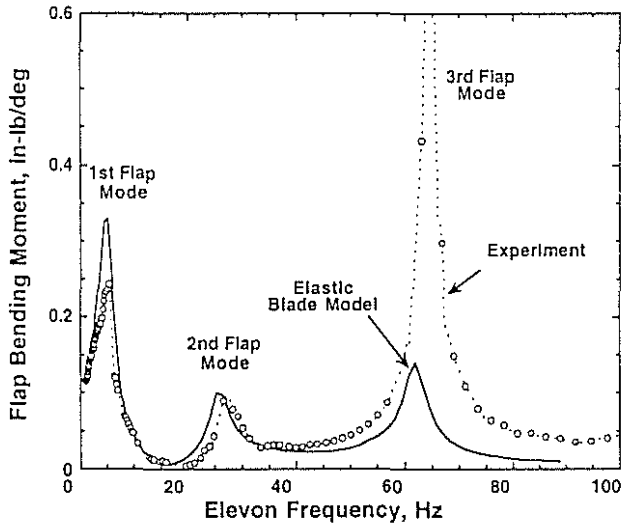

Fig. 21a Flap bending moment FRF magnitude in hover, comparison of elastic blade analysis with experiment, 200 RPM.

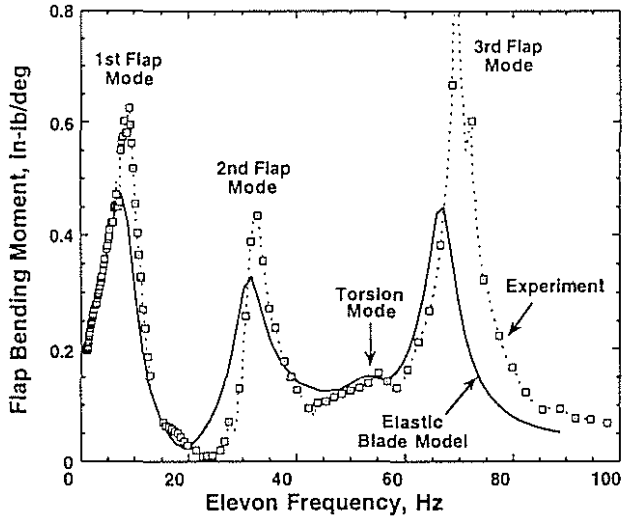

Fig. 21b Flap bending moment FRF magnitude in hover, comparison of elastic blade analysis with experiment, 425 RPM.

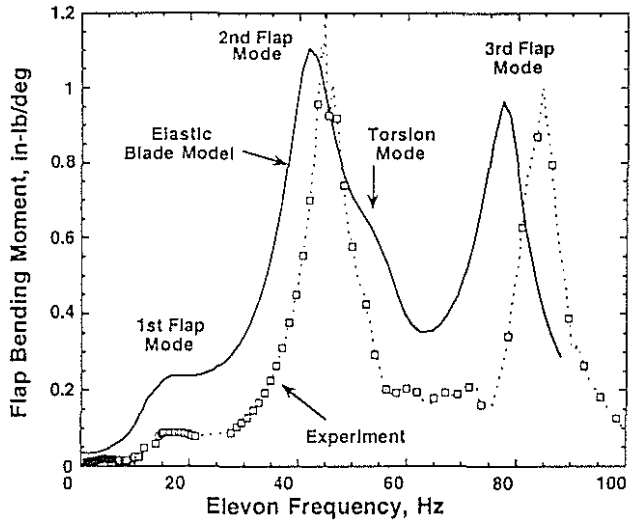

Fig. 21c Flap bending FRF magnitude, in hover, comparing analysis and experiment, 760 RPM.

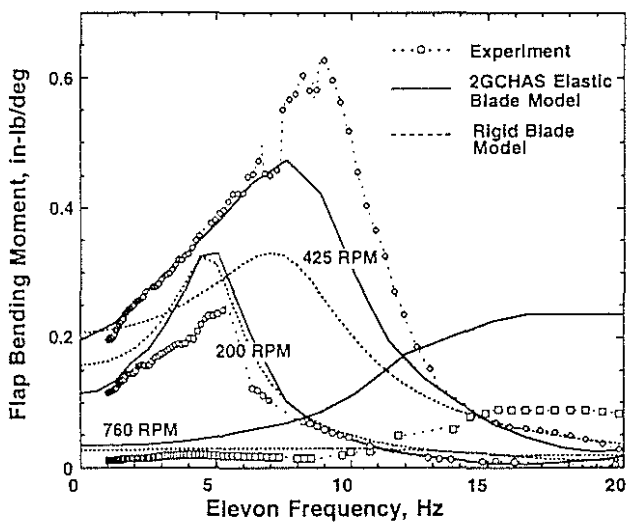

Fig. 22 Flap bending moment comparisons of elastic and rigid blade analyses with experiment at low frequencies.

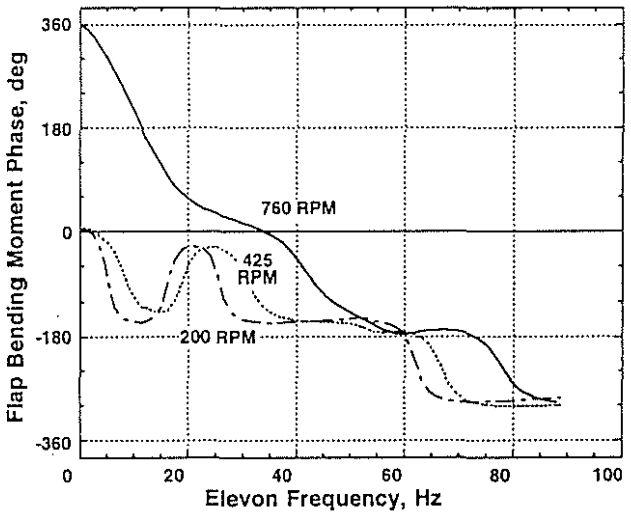

Fig. 23a Flap bending moment FRF phase in hover from elastic blade analysis; compare with Fig. 23b.

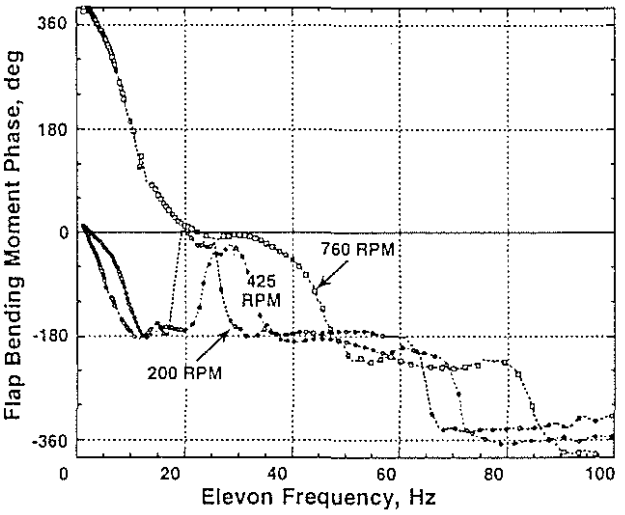

Fig. 23b Experimental flap bending moment FRF phase in hover; compare with Fig. 23a.

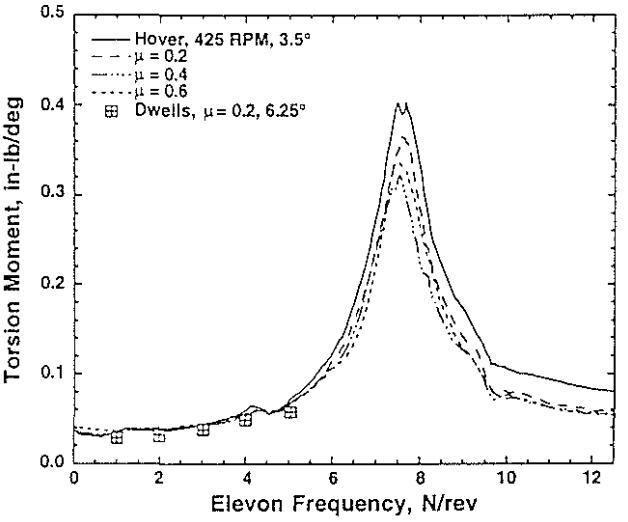

Fig. 26 Effect of advance ratio on experimental torsion moment FRF, 450 RPM, θ_o = 0 deg.

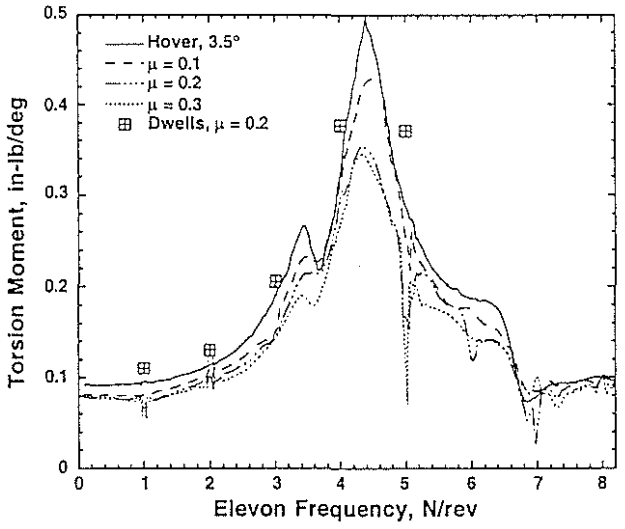

Fig. 24 Effect of advance ratio on experimental torsion moment FRF, 760 RPM, θ_o = 4 deg.

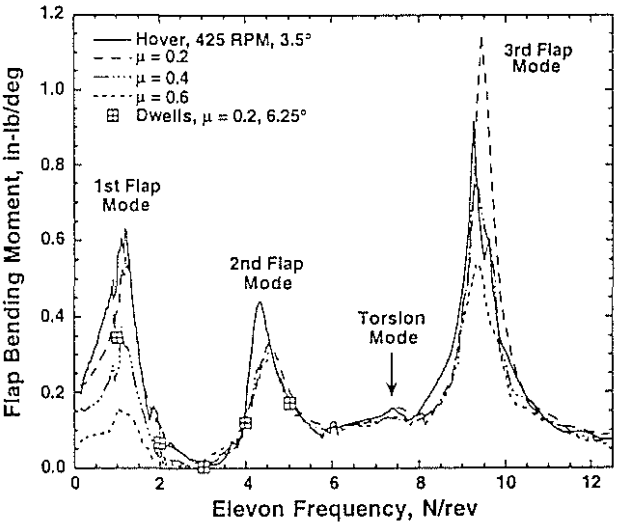

Fig. 27 Effect of advance ratio on experimental flap bending moment FRF, 450 RPM, θ_o = 0 deg.

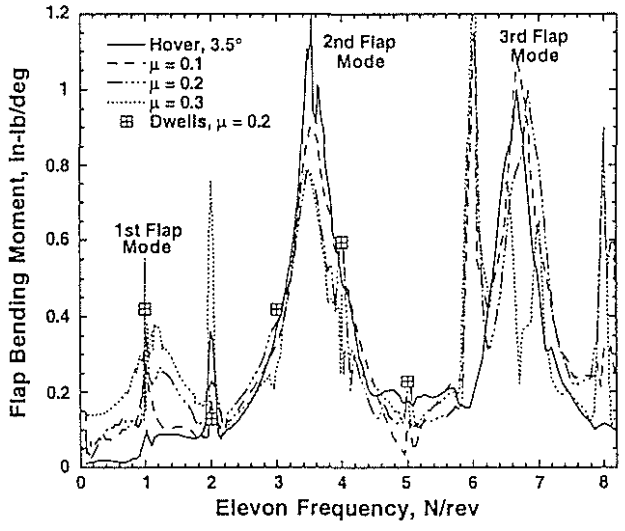

Fig. 25 Effect of advance ratio on experimental flap bending moment FRF, 760 RPM, θ_o = 4 deg.

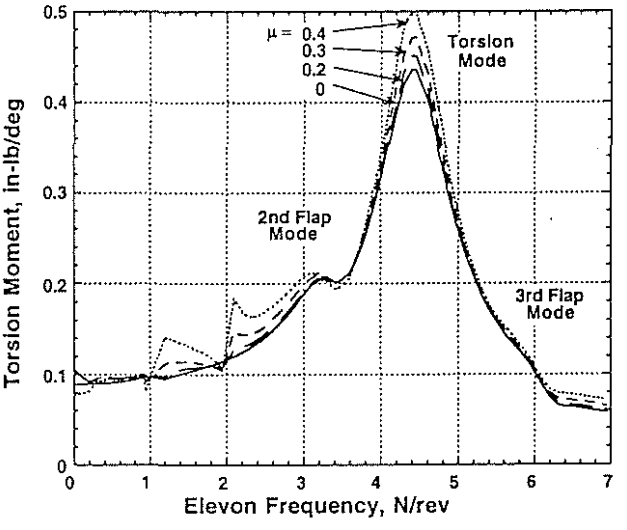

Fig. 28 Torsion moment FRF magnitude in forward flight, elastic blade analysis, 760 RPM.

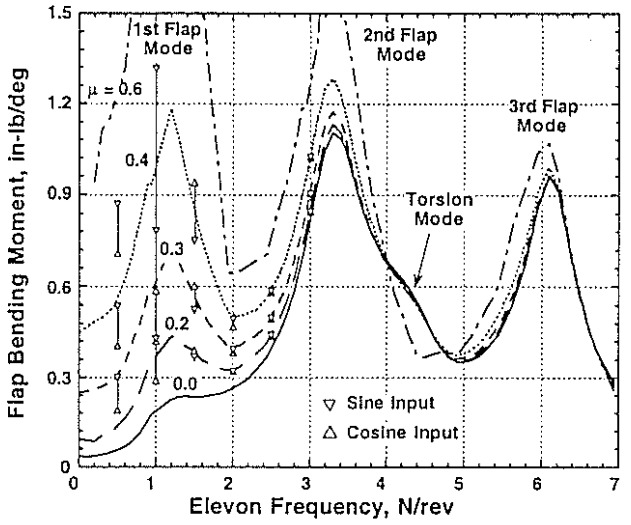

Fig. 29 Flap bending moment FRF magnitude in forward flight, elastic blade analysis, 760 RPM.

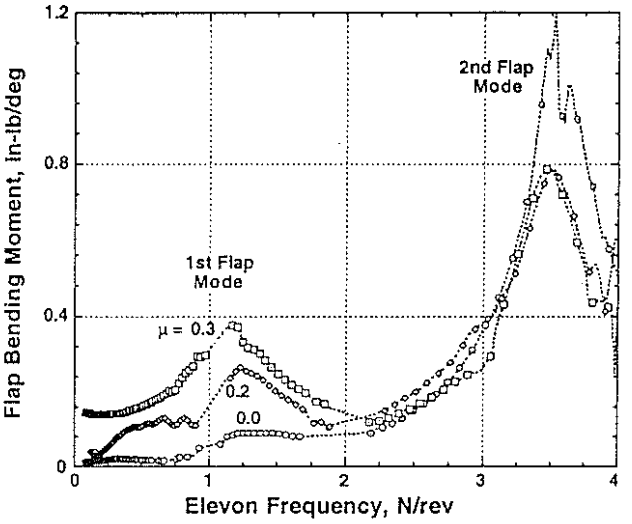

Fig. 30b Experimental flap bending moment FRF magnitude in forward flight, compare with Fig. 30a.

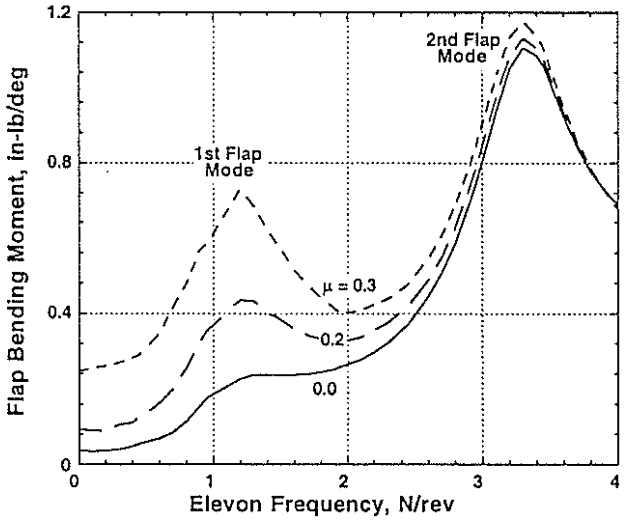

Fig. 30a Flap bending moment FRF magnitude in forward flight, elastic blade analysis, 760 RPM, low frequency range; compare with Fig. 30b.